Supplementary Information

Crystalline structure-dielectric property relationship in combustion-synthesized barium titanate nanocrystals with different sizes

Qiong Li [1], Tianxiong Ju [1], Ruipeng Li [2], Shuang Wang [3], Yongfang Yang [3], Hatsuo Ishida [1], Yeu-Wei Harn [4], Jihua Chen [5], Benjamin Hirt [6], Alp Sehirlioglu [6], Zhiqun Lin [7,*], and Lei Zhu [1,*]

[1] Department of Macromolecular Science and Engineering, Case Western Reserve University, Cleveland, Ohio 44106, United States
[2] National Synchrotron Light Source II, Brookhaven National Laboratory, Upton, New York 11973, United States
[3] Institute of Polymer Science and Engineering, Hebei Key Laboratory of Functional Polymers, Hebei University of Technology, Tianjin 300130, P. R. China
[4] School of Materials Science and Engineering, Georgia Institute of Technology, Atlanta, Georgia 30332, United States
[5] Center for Nanophase Materials Sciences, Oak Ridge National Laboratory, Oak Ridge, Tennessee 37831, United States
[6] Department of Materials Science and Engineering, Case Western Reserve University, Cleveland, Ohio 44106, United States
[7] Department of Chemical and Biomolecular Engineering, National University of Singapore, Singapore 117585, Singapore

* Corresponding authors. Emails: lxz121@case.edu (L.Z.) and z.lin@nus.edu.sg (Z.L.)

1. FTIR study of arBTO nanocrystals

FTIR measurements were performed for arBTO50-arBTO500 nanocrystals. The measurements were carried out at the ambient condition. The arBTO nanocrystals were dried in a vacuum oven at 80 °C overnight prior to the measurement to reduce the moisture absorption. Besides the Ti-O peak at 486 cm^{-1} and the Ba-Ti-O peak at 1450 cm^{-1}, diamond crystal absorption at 1900-2240 cm^{-1} and CO_2 peaks around 2346 cm^{-1} were also observed. No other absorption bands were seen from other chemical substances. With increasing the particle size, increased light scattering was noticed above 2000 cm^{-1}.

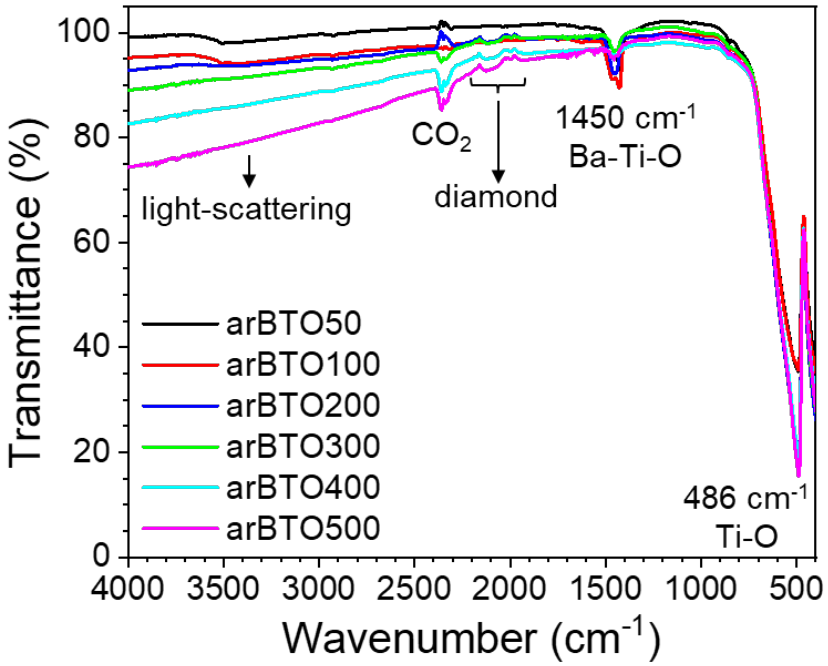

Fig. S1. ATR FTIR spectra of arBTO50-arBTO500 nanocrystals using the single-bounce diamond crystal.

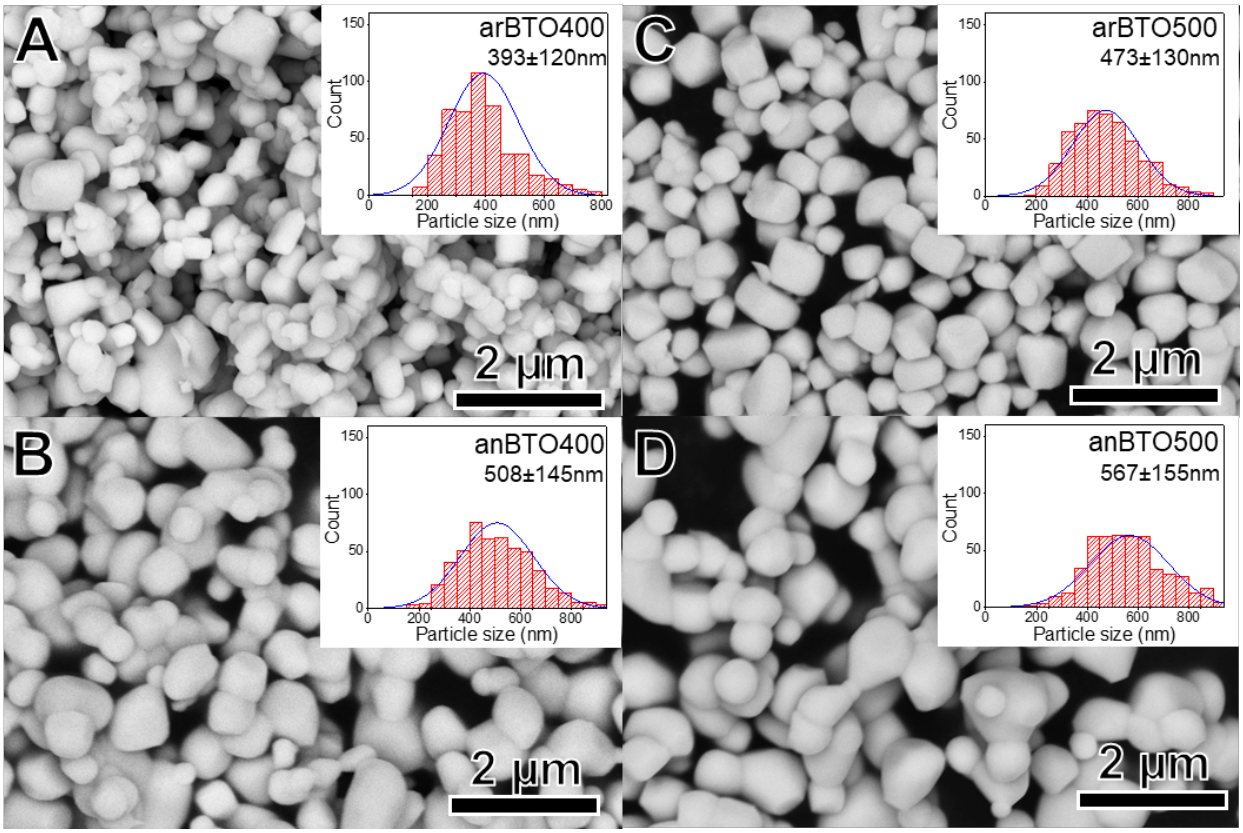

Fig. S2. SEM micrographs of (A) arBTO400, (B) anBTO400, (C) arBTO500, (D) anBTO500. The insets show particle-size histograms and the mean particle size with error (i.e., mean ± standard deviation).

2. DSC and SEM analyses to determine the optimal annealing temperature

SEM micrographs of arBTO400, anBTO400, arBTO500, and anBTO500 are shown in Figs. S2A-D, respectively. The insets show the particle size histograms obtained by counting over 500 particles for each sample. The averaged particle sizes were 393±120 nm for arBTO400 and 473±130 nm for arBTO500 nanocrystals, while the corresponding 950 °C-annealed particle sizes were 473±130 nm for anBTO400 and 567±155 nm for anBTO500 nanocrystals, which were equivalent to 29% and 20% increase, respectively.

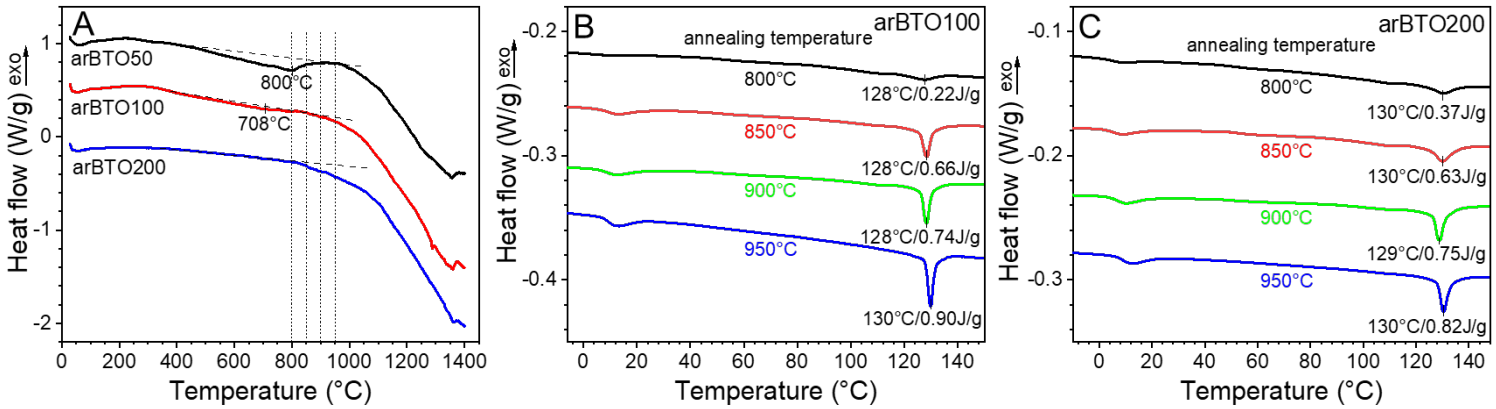

Fig. S3. (A) High-temperature DSC of arBTO50, arBTO100, and arBTO200 nanocrystals. Heating curves of conventional DSC for (B) arBTO100 (C) arBTO200 after 800-950 °C annealing for 72 h.

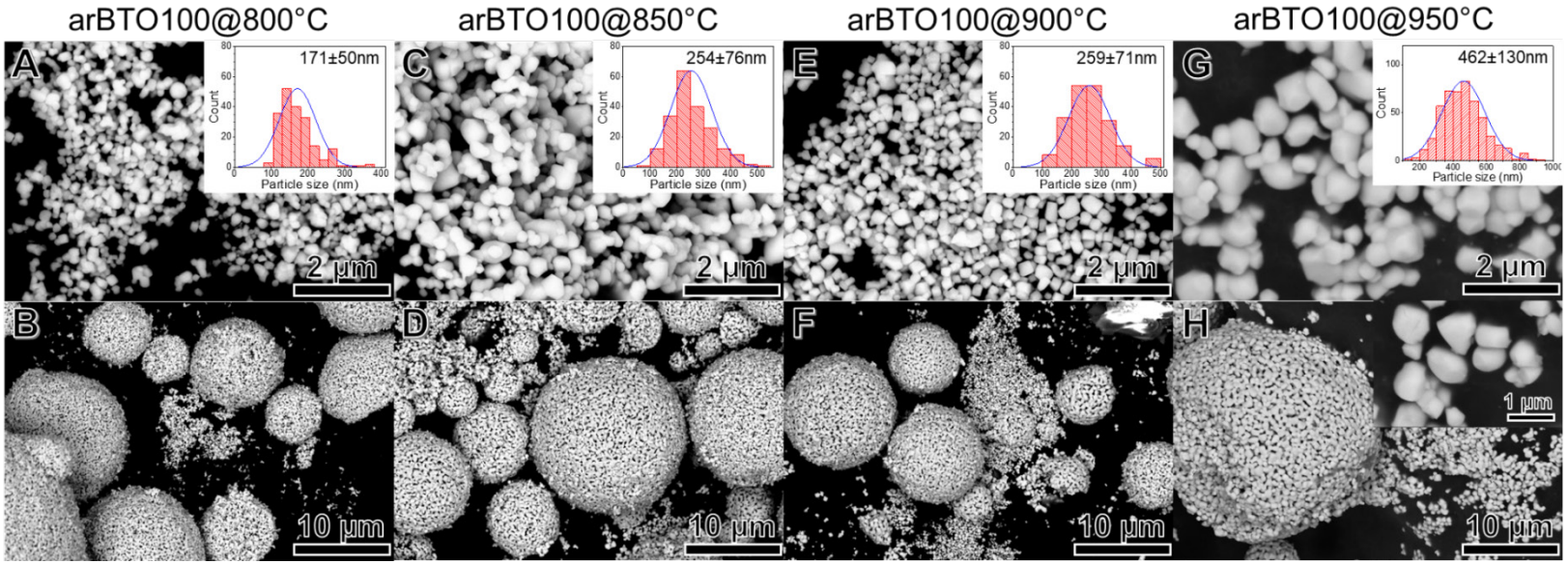

Fig. S4. SEM micrographs of arBTO100 nanocrystals after annealing at (A) 800 °C, (C) 850 °C, (E) 900 °C, (G) 950 °C (i.e., anBTO100) for 72 h. The corresponding low magnification micrographs are shown in (B, D, F, H), respectively. The insets show particle-size histograms and the averaged particle size with error (i.e., mean ± standard deviation).

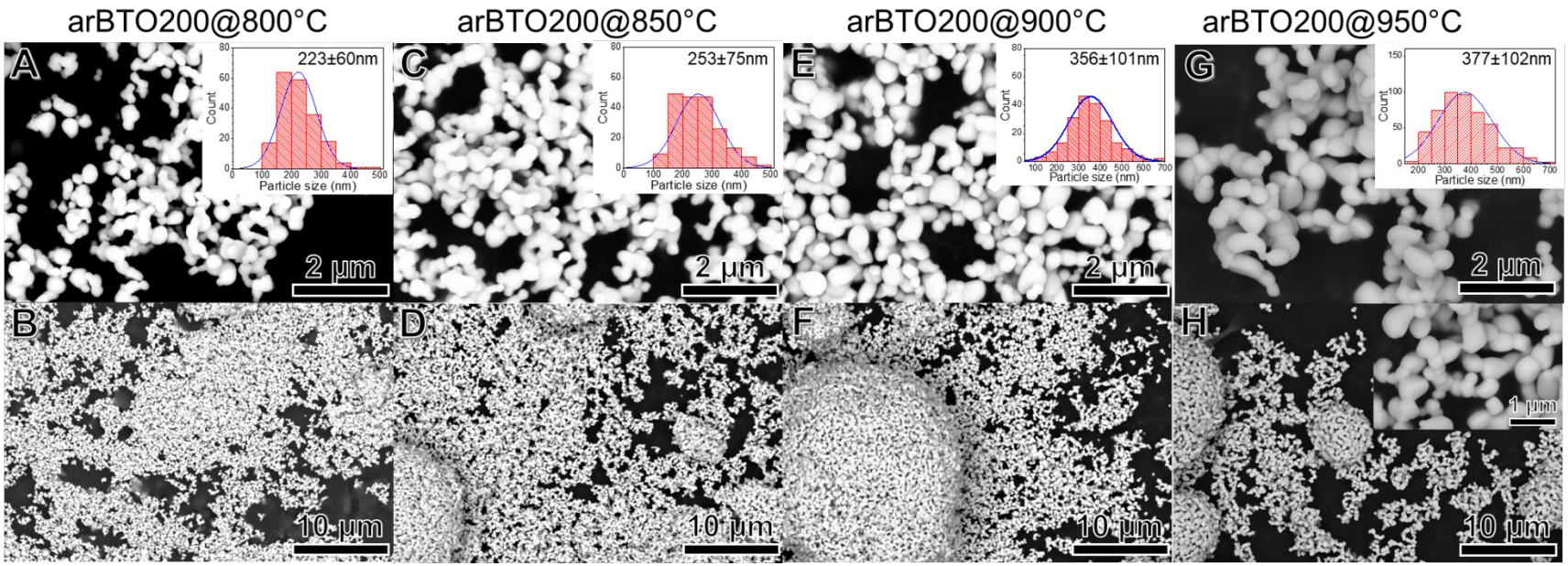

Fig. S5. SEM micrographs of arBTO200 nanocrystals after annealing at (A) 800 °C, (C) 850 °C, (E) 900 °C, and (G) 950 °C for 72 h. The corresponding low magnification micrographs are shown in (B, D, F, H), respectively. The insets show particle-size histograms and the averaged particle size with error (i.e., mean ± standard deviation).

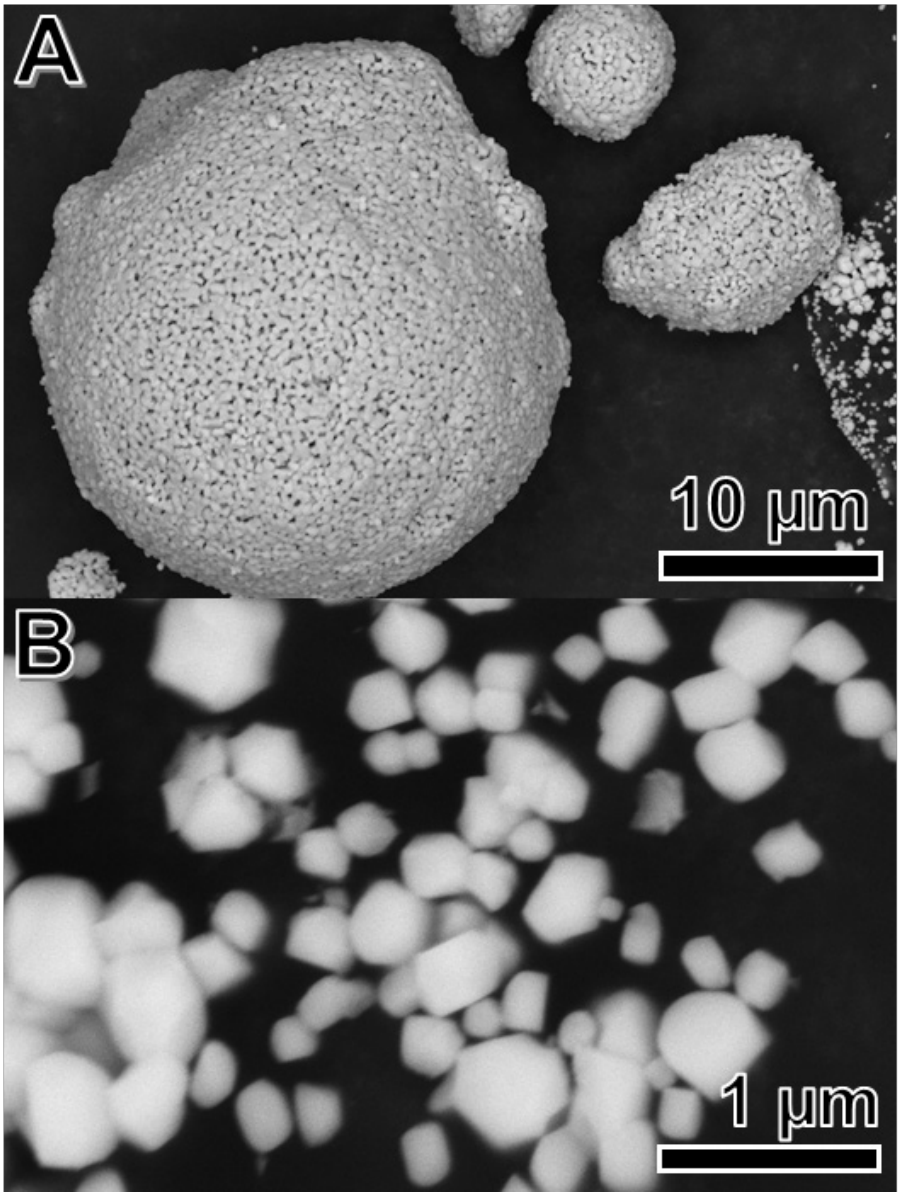

Fig. S6. SEM micrographs of arBTO50 thermally annealed at 950 °C for 72 h, i.e., anBTO50: (A) low and (B) high magnifications. Some particles have sintered into ~800 nm particles.

3. XRD characterization of BTO nanocrystals

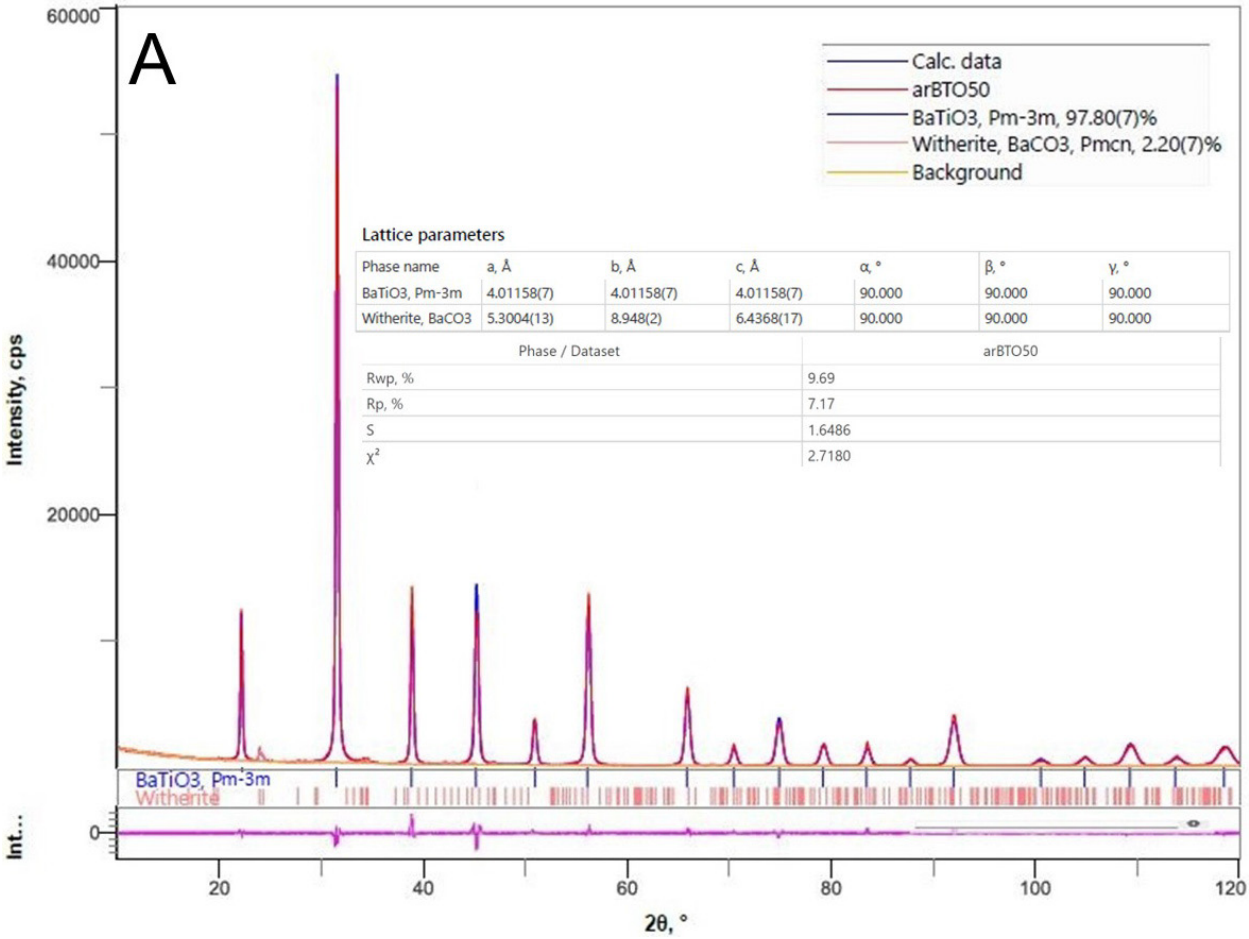

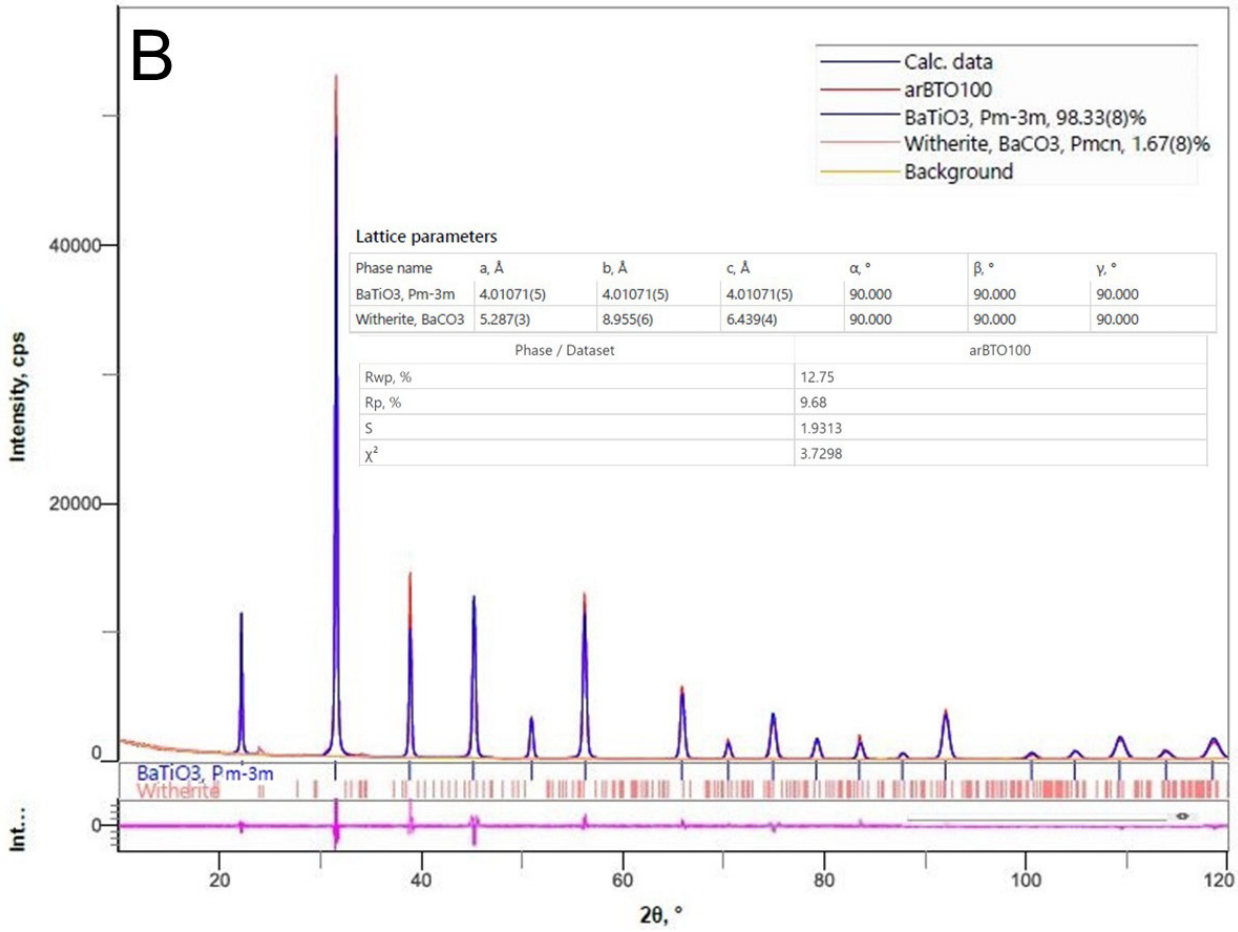
B
Calc. data
arBTO100
BaTiO3, Pm-3m, 98.33(8)%
Witherite, BaCO3, Pmcn, 1.67(8)%
Background
Lattice parameters
Phase name | a, Å | b, Å | c, Å | α, ° | β, ° | γ, °
BaTiO3, Pm-3m | 4.01071(5) | 4.01071(5) | 4.01071(5) | 90.000 | 90.000 | 90.000
Witherite, BaCO3 | 5.287(3) | 8.955(6) | 6.439(4) | 90.000 | 90.000 | 90.000
Phase / Dataset | arBTO100
Rwp, % | 12.75
Rp, % | 9.68
S | 1.9313
χ² | 3.7298
Intensity, cps
40000
20000
0
BaTiO3, Pm-3m
Witherite
Int...
0
20
40
60
80
100
120
2θ, °

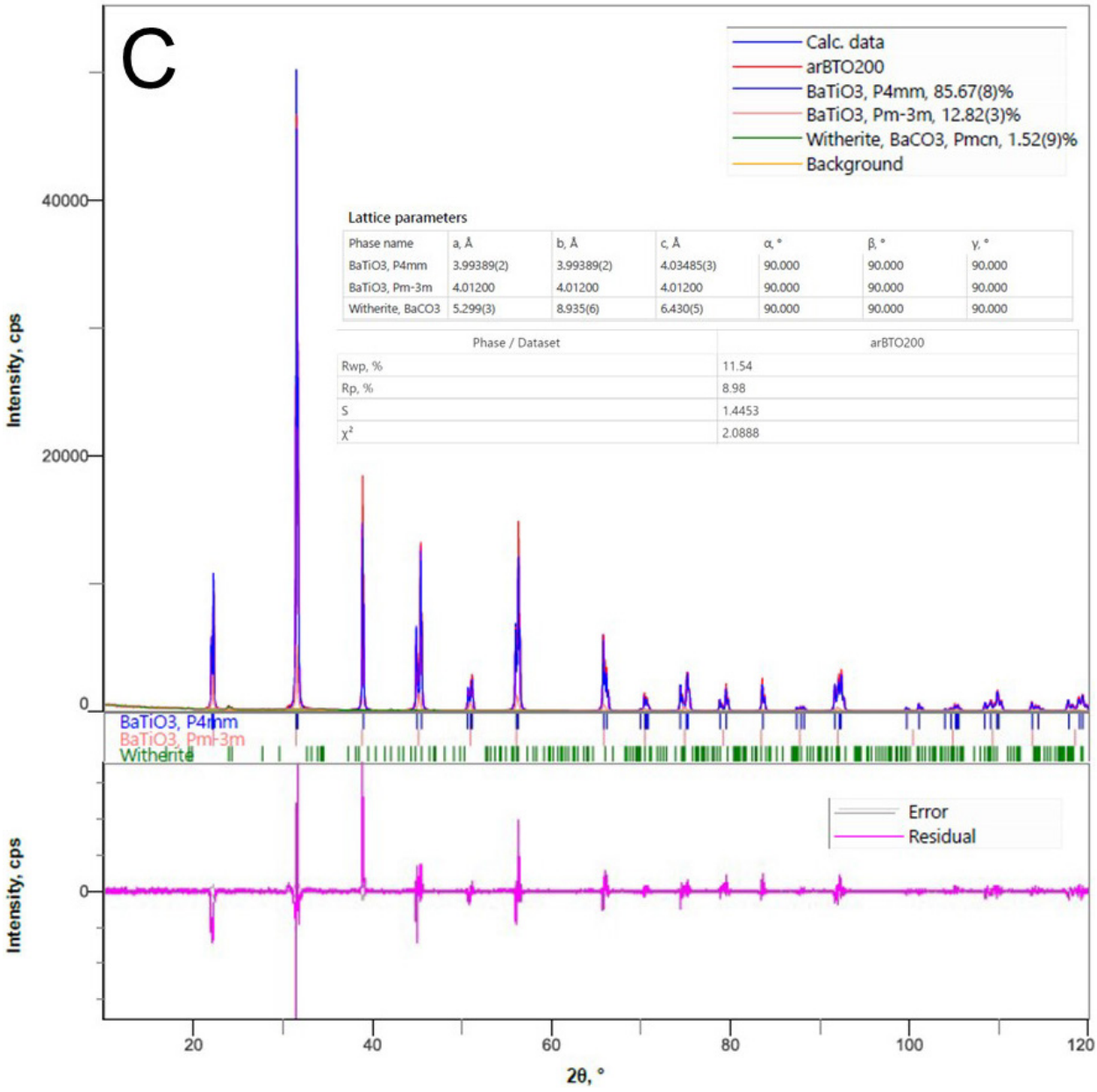
C
Calc. data
arBTO200
BaTiO3, P4mm, 85.67(8)%
BaTiO3, Pm-3m, 12.82(3)%
Witherite, BaCO3, Pmcn, 1.52(9)%
Background
Lattice parameters
Phase name | a, Å | b, Å | c, Å | α, ° | β, ° | γ, °
BaTiO3, P4mm | 3.99389(2) | 3.99389(2) | 4.03485(3) | 90.000 | 90.000 | 90.000
BaTiO3, Pm-3m | 4.01200 | 4.01200 | 4.01200 | 90.000 | 90.000 | 90.000
Witherite, BaCO3 | 5.299(3) | 8.935(6) | 6.430(5) | 90.000 | 90.000 | 90.000
Phase / Dataset | arBTO200
Rwp, % | 11.54
Rp, % | 8.98
S | 1.4453
χ² | 2.0888
Intensity, cps
40000
20000
0
BaTiO3, P4mm
BaTiO3, Pm-3m
Witherite
Error
Residual
Intensity, cps
0
20
40
60
80
100
120
2θ, °

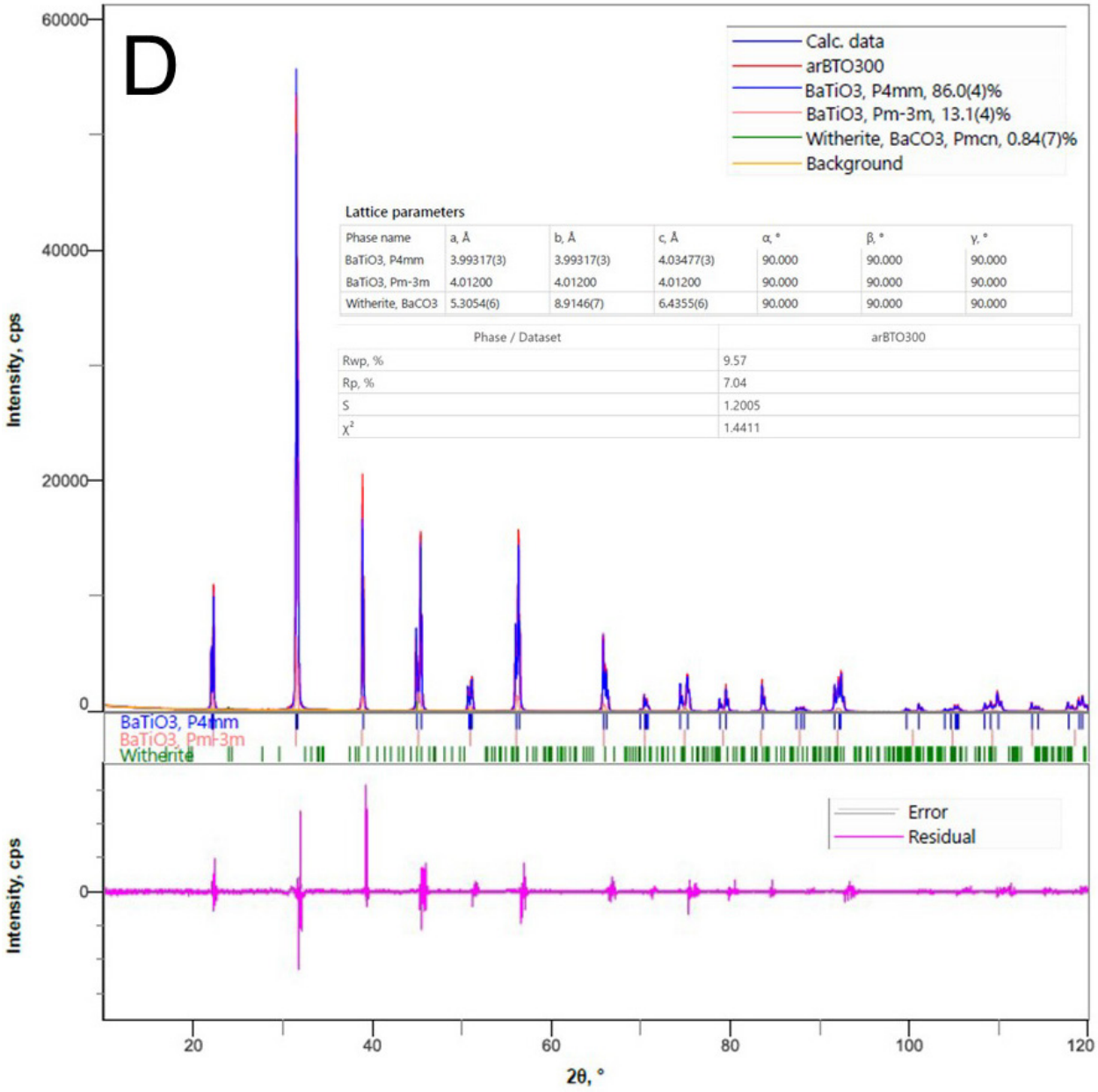
D
Calc. data
arBTO300
BaTiO3, P4mm, 86.0(4)%
BaTiO3, Pm-3m, 13.1(4)%
Witherite, BaCO3, Pmcn, 0.84(7)%
Background
Lattice parameters
Phase name | a, Å | b, Å | c, Å | α, ° | β, ° | γ, °
BaTiO3, P4mm | 3.99317(3) | 3.99317(3) | 4.03477(3) | 90.000 | 90.000 | 90.000
BaTiO3, Pm-3m | 4.01200 | 4.01200 | 4.01200 | 90.000 | 90.000 | 90.000
Witherite, BaCO3 | 5.3054(6) | 8.9146(7) | 6.4355(6) | 90.000 | 90.000 | 90.000
Phase / Dataset | arBTO300
Rwp, % | 9.57
Rp, % | 7.04
S | 1.2005
χ² | 1.4411
Intensity, cps
60000
40000
20000
0
BaTiO3, P4mm
BaTiO3, Pm-3m
Witherite
Error
Residual
Intensity, cps
0
20
40
60
80
100
120
2θ, °

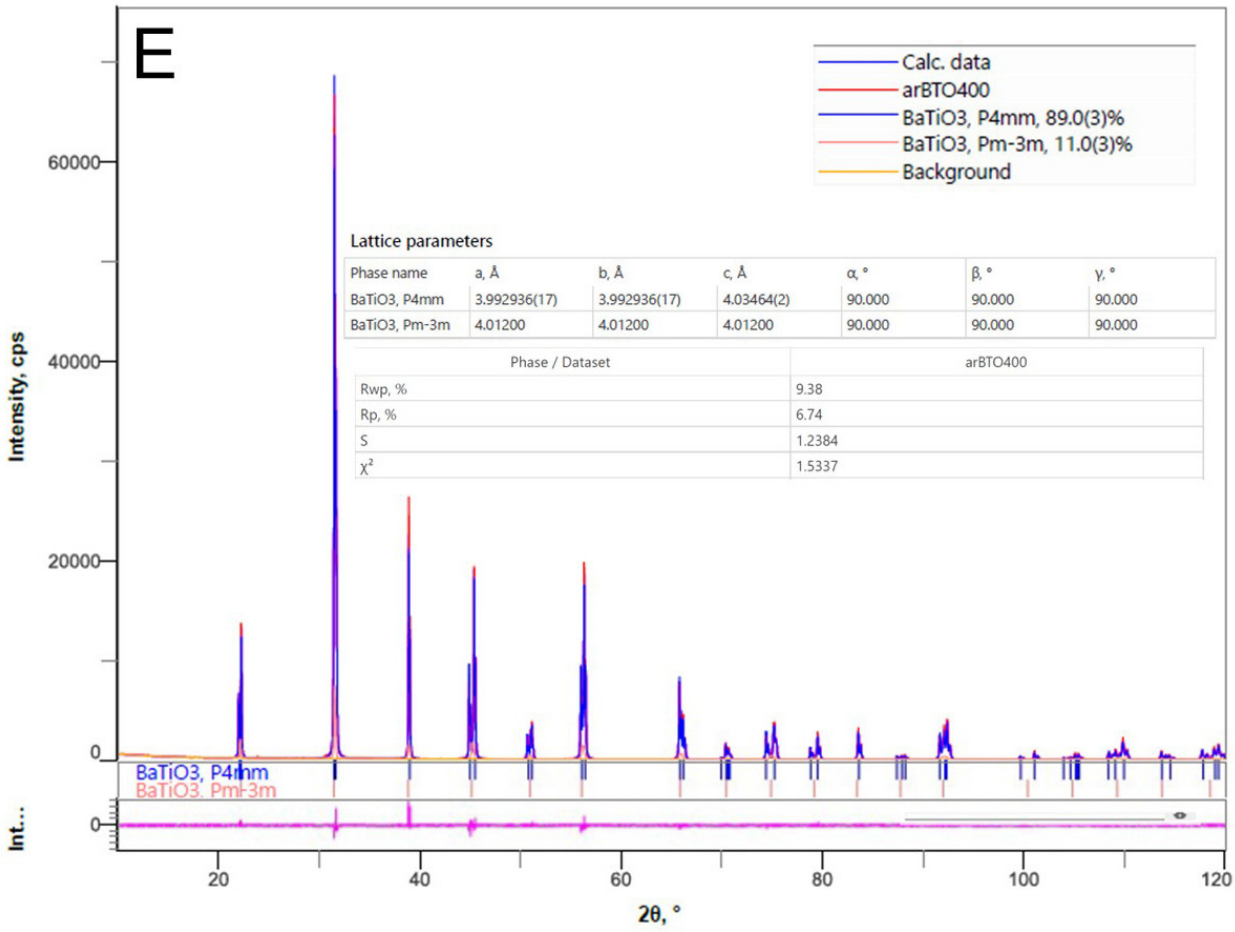
E
Calc. data
arBTO400
BaTiO3, P4mm, 89.0(3)%
BaTiO3, Pm-3m, 11.0(3)%
Background
Lattice parameters
Phase name | a, Å | b, Å | c, Å | α, ° | β, ° | γ, °
BaTiO3, P4mm | 3.992936(17) | 3.992936(17) | 4.03464(2) | 90.000 | 90.000 | 90.000
BaTiO3, Pm-3m | 4.01200 | 4.01200 | 4.01200 | 90.000 | 90.000 | 90.000
Phase / Dataset | arBTO400
Rwp, % | 9.38
Rp, % | 6.74
S | 1.2384
χ² | 1.5337
Intensity, cps
60000
40000
20000
0
BaTiO3, P4mm
BaTiO3, Pm-3m
Int...
0
20
40
60
80
100
120
2θ, °

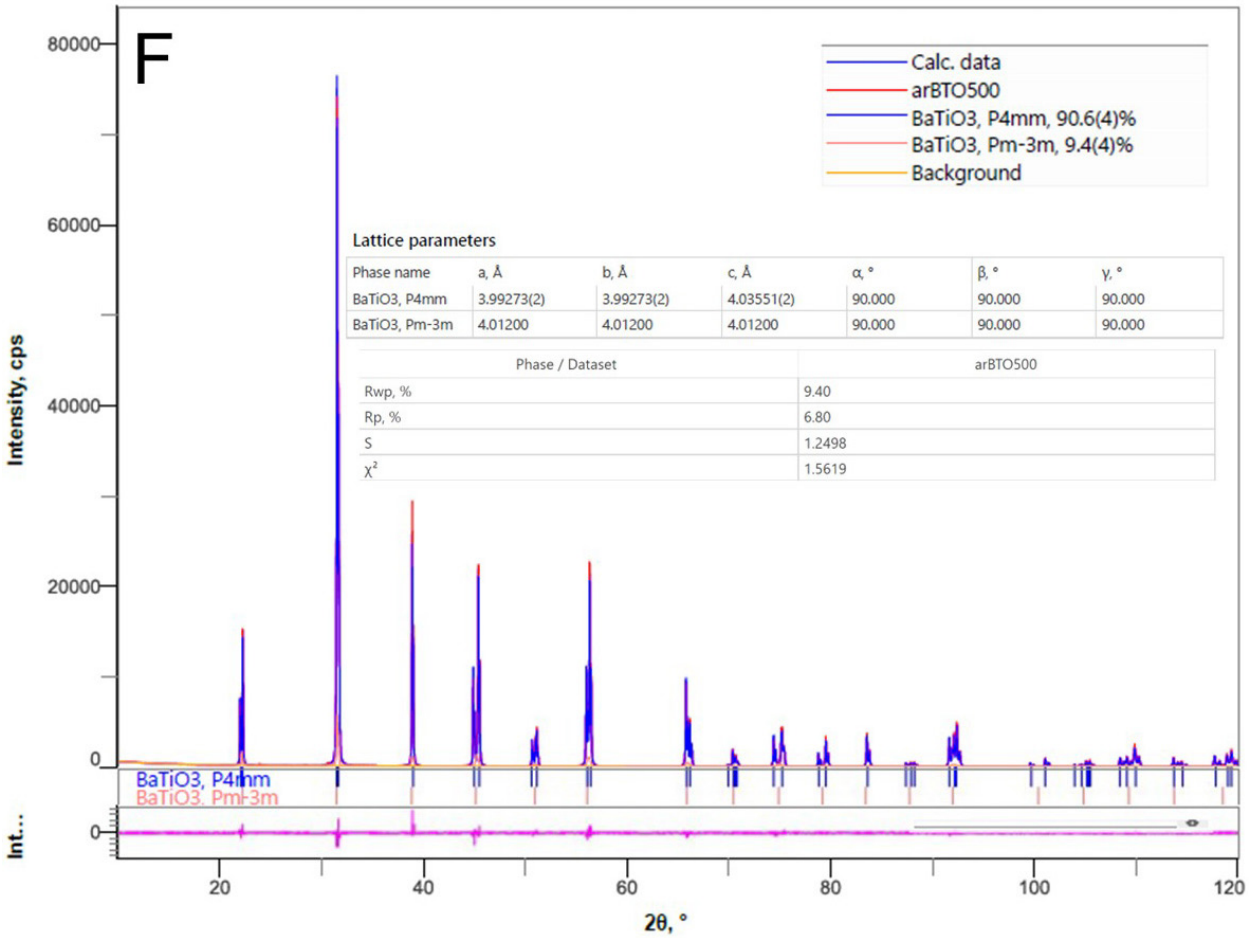

Fig. S7. Powder XRD profiles and Rietveld fitting results for arBTO50-arBTO500 nanocrystals at room temperature. The contents of tetragonal and cubic $BaTiO_3$, and witherite $BaCO_3$ are shown. The fitted lattice parameters for different crystal structures are presented.

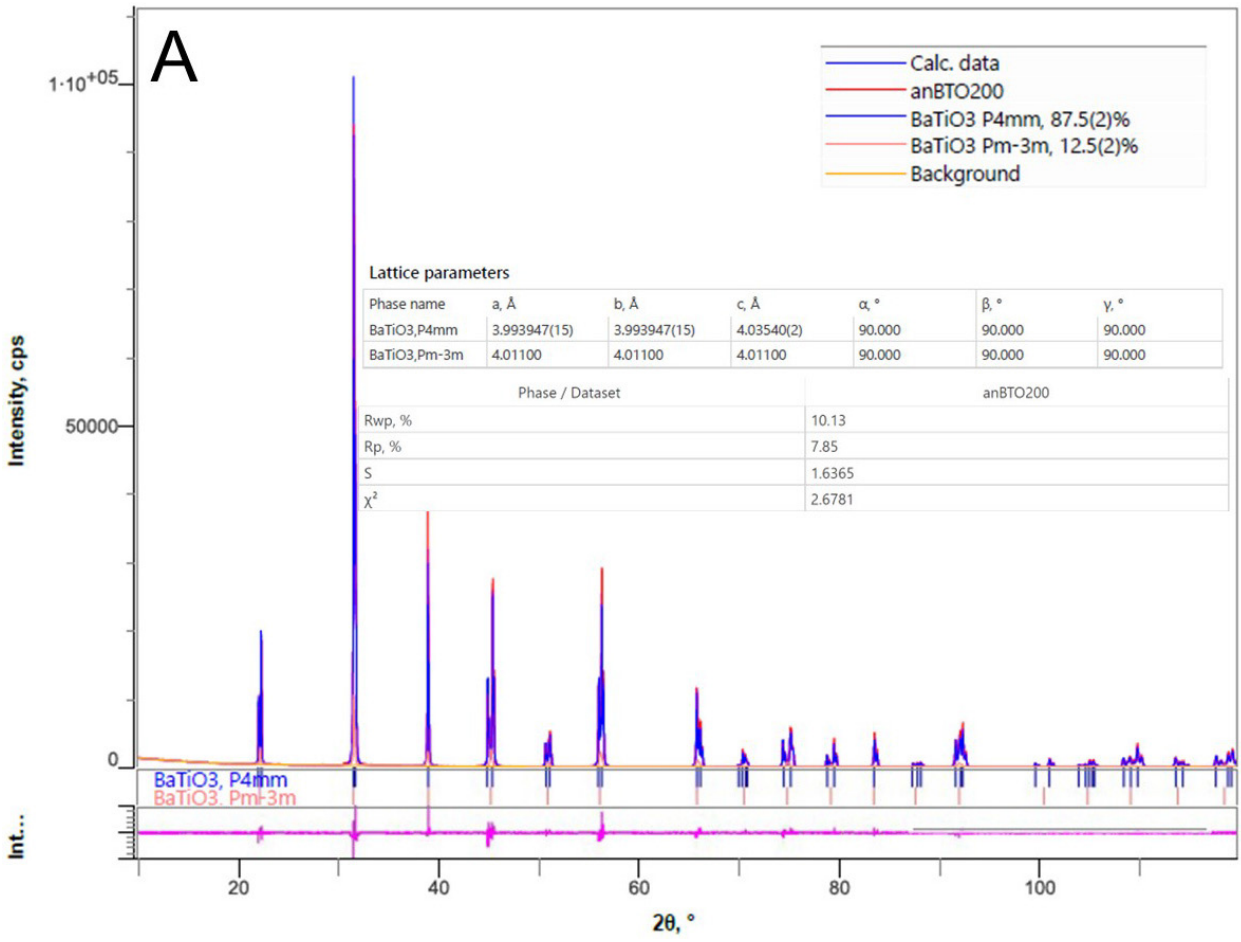
A
Calc. data
anBTO200
BaTiO3 P4mm, 87.5(2)%
BaTiO3 Pm-3m, 12.5(2)%
Background
Lattice parameters
Phase name | a, Å | b, Å | c, Å | α, ° | β, ° | γ, °
BaTiO3,P4mm | 3.993947(15) | 3.993947(15) | 4.03540(2) | 90.000 | 90.000 | 90.000
BaTiO3,Pm-3m | 4.01100 | 4.01100 | 4.01100 | 90.000 | 90.000 | 90.000
Phase / Dataset | anBTO200
Rwp, % | 10.13
Rp, % | 7.85
S | 1.6365
χ² | 2.6781
Intensity, cps
1·10+05
50000
0
BaTiO3, P4mm
BaTiO3, Pm-3m
Int...
20
40
60
80
100
2θ, °

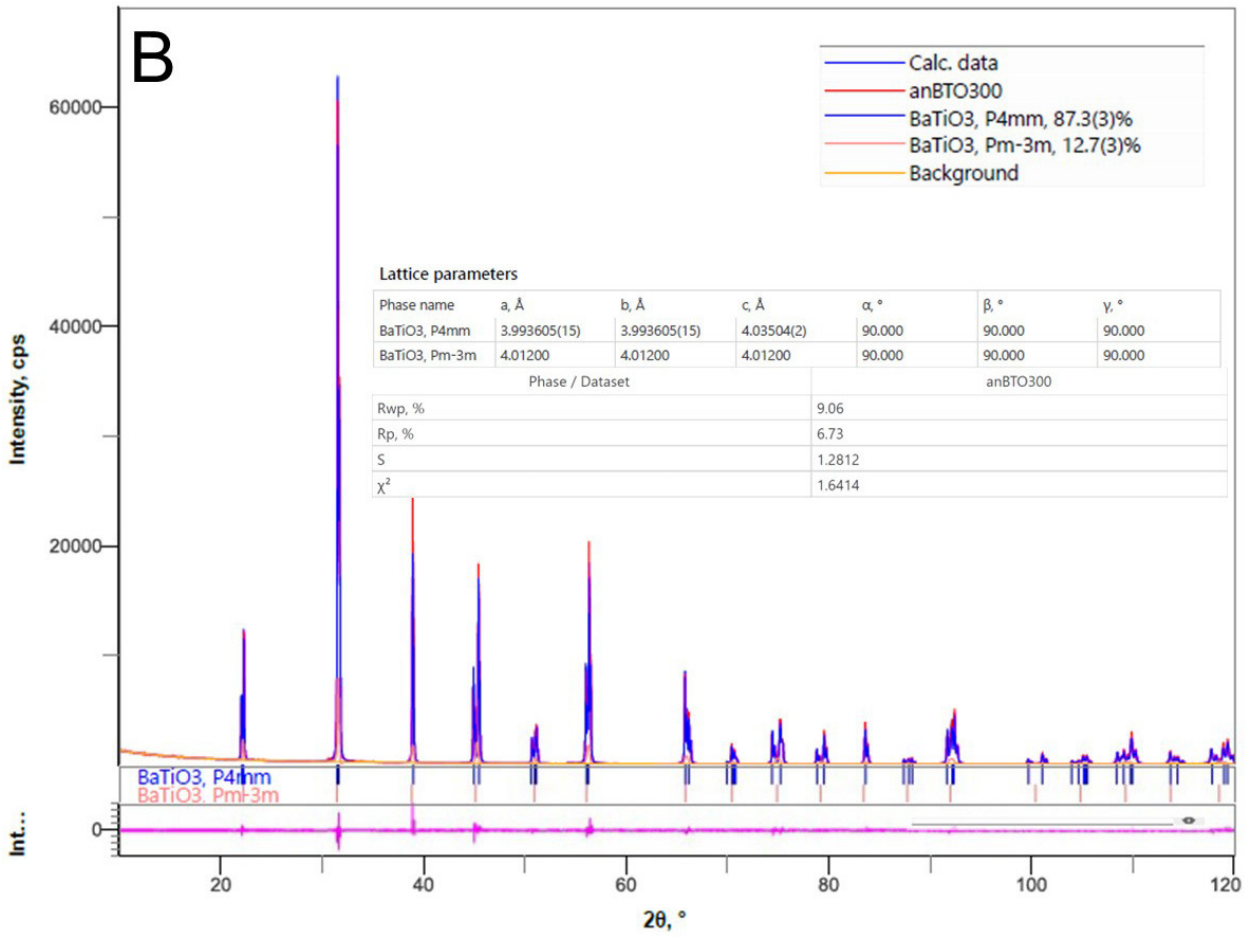
B
Calc. data
anBTO300
BaTiO3, P4mm, 87.3(3)%
BaTiO3, Pm-3m, 12.7(3)%
Background
Lattice parameters
Phase name | a, Å | b, Å | c, Å | α, ° | β, ° | γ, °
BaTiO3, P4mm | 3.993605(15) | 3.993605(15) | 4.03504(2) | 90.000 | 90.000 | 90.000
BaTiO3, Pm-3m | 4.01200 | 4.01200 | 4.01200 | 90.000 | 90.000 | 90.000
Phase / Dataset | anBTO300
Rwp, % | 9.06
Rp, % | 6.73
S | 1.2812
χ² | 1.6414
Intensity, cps
60000
40000
20000
BaTiO3, P4mm
BaTiO3, Pm-3m
Int...
0
20
40
60
80
100
120
2θ, °

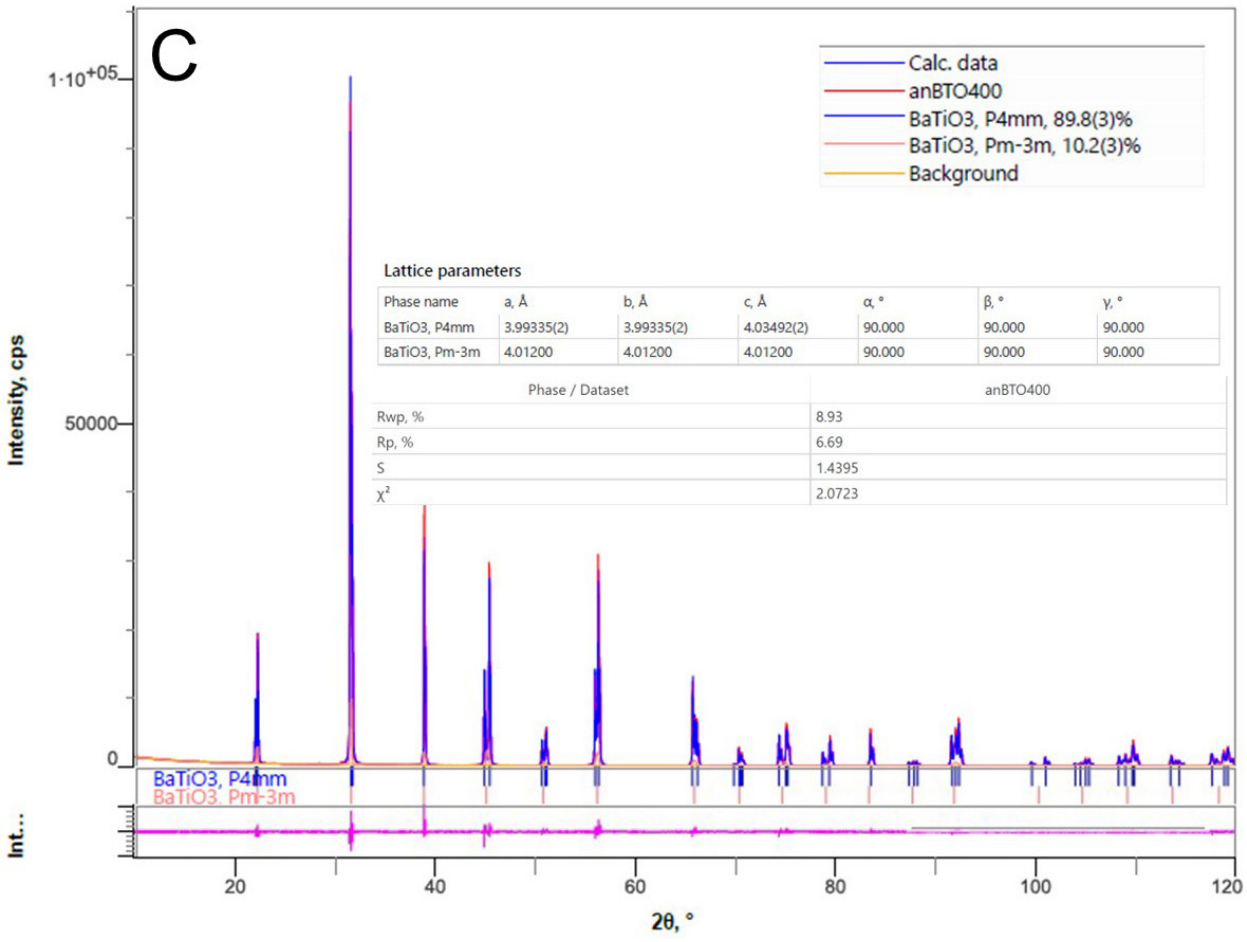
C
Calc. data
anBTO400
BaTiO3, P4mm, 89.8(3)%
BaTiO3, Pm-3m, 10.2(3)%
Background
Lattice parameters
Phase name | a, Å | b, Å | c, Å | α, ° | β, ° | γ, °
BaTiO3, P4mm | 3.99335(2) | 3.99335(2) | 4.03492(2) | 90.000 | 90.000 | 90.000
BaTiO3, Pm-3m | 4.01200 | 4.01200 | 4.01200 | 90.000 | 90.000 | 90.000
Phase / Dataset | anBTO400
Rwp, % | 8.93
Rp, % | 6.69
S | 1.4395
χ² | 2.0723
Intensity, cps
1·10+05
50000
0
BaTiO3, P4mm
BaTiO3, Pm-3m
Int...
20
40
60
80
100
120
2θ, °

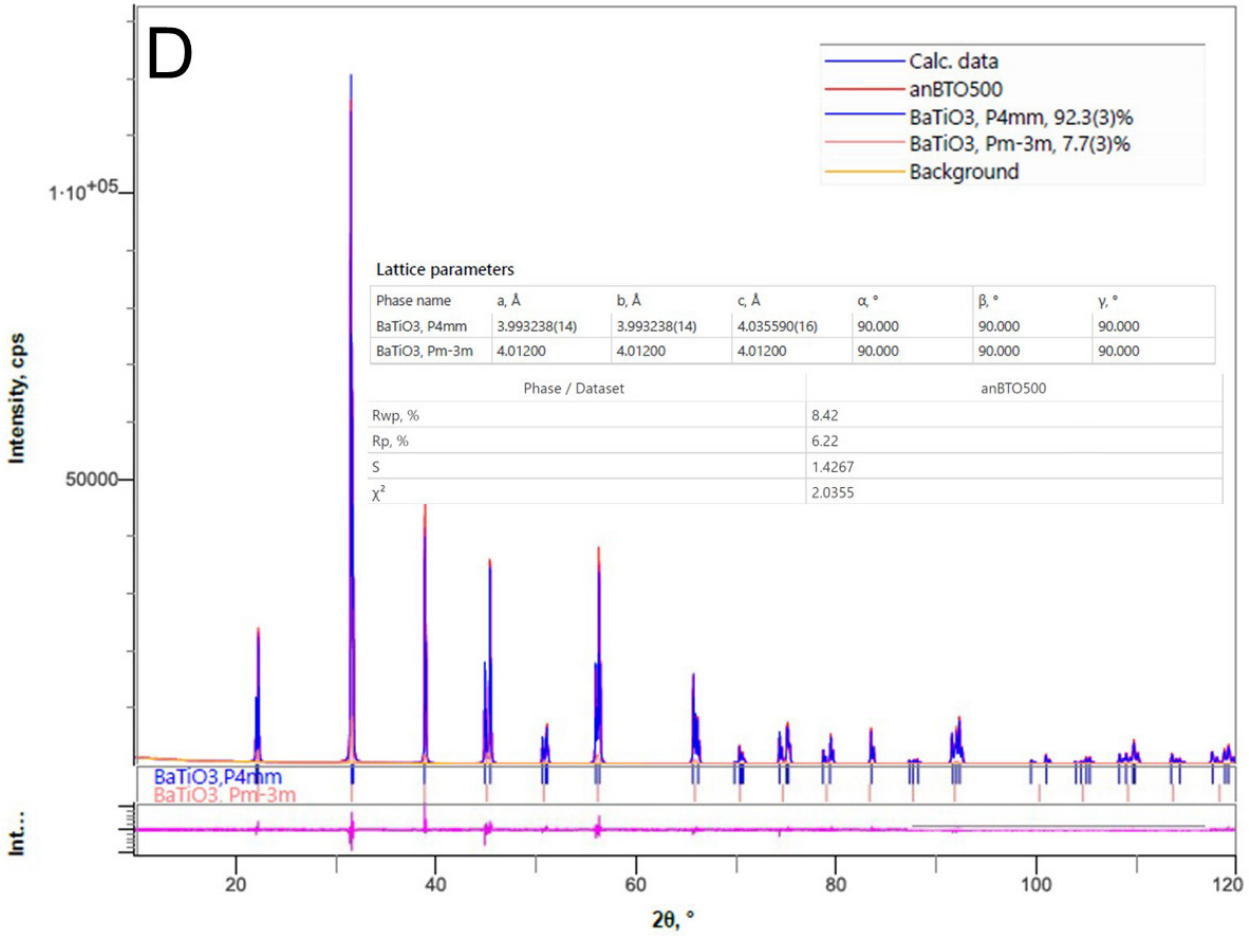

Fig. S8. Powder XRD profiles and Rietveld fitting results for arBTO50-arBTO500 nanocrystals at room temperature. The contents of tetragonal and cubic $BaTiO_3$, and witherite $BaCO_3$ are shown. The fitted lattice parameters for different crystal structures are presented.

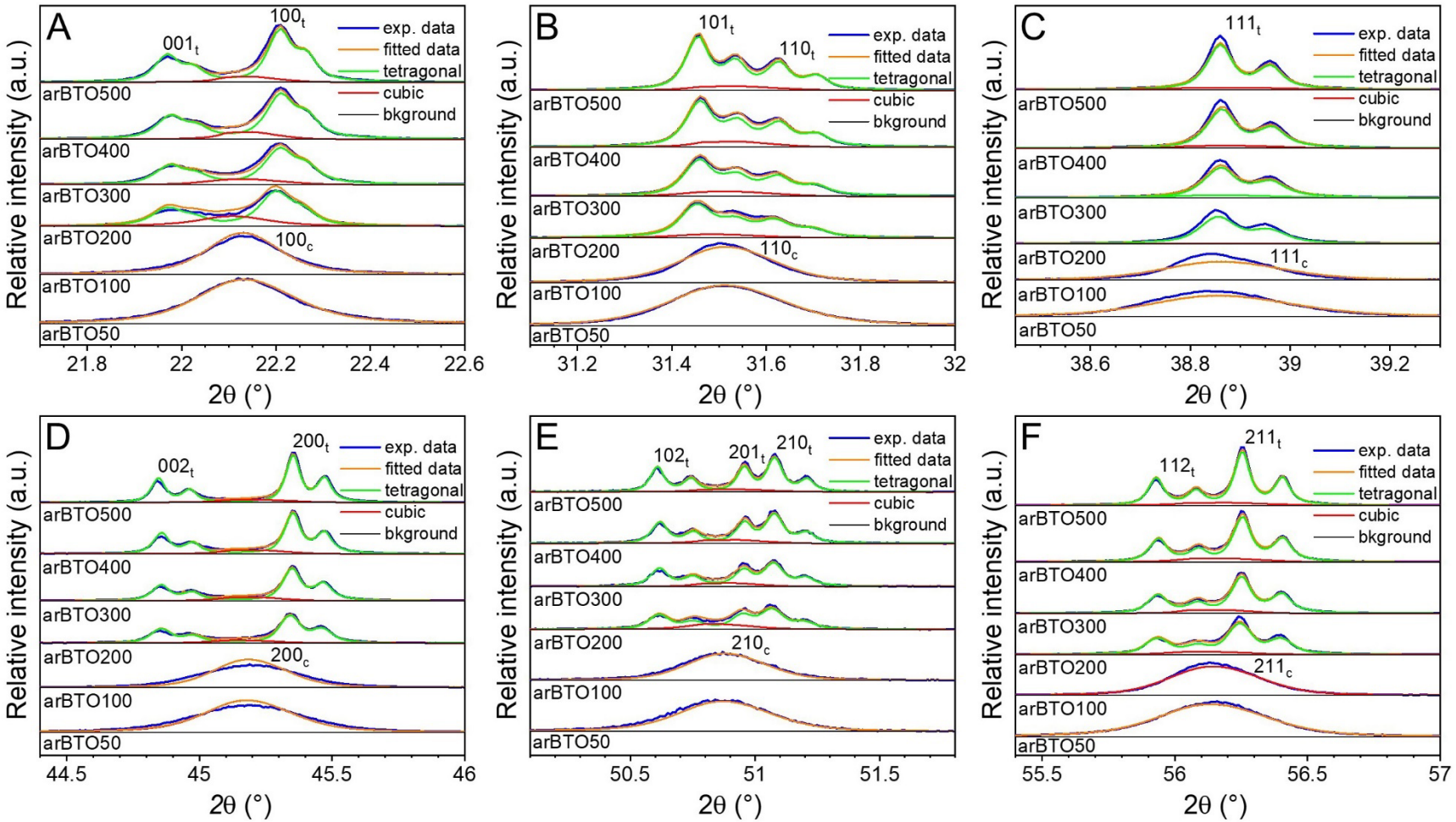

Fig. S9. Detailed Rietveld fitting results for the first 6 reflections of arBTO50-arBTO500 nanocrystals at room temperature. The splitting of tetragonal peaks is attributed to the Cu $K_{\alpha 1}$ and $K_{\alpha 2}$ radiations in the X-ray source.

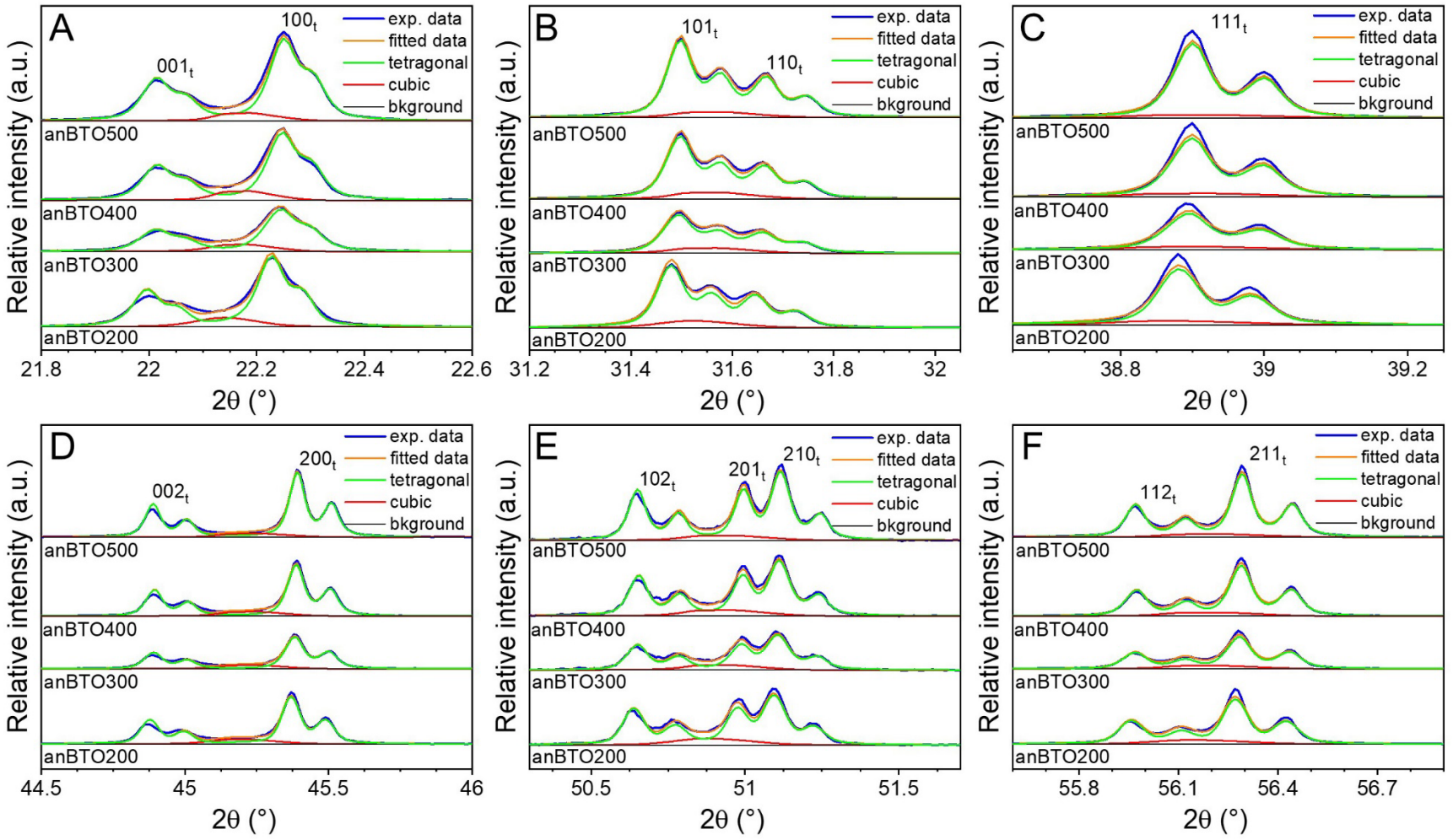

Fig. S10. Detailed Rietveld fitting results for the first 6 reflections of anBTO200-anBTO500 nanocrystals at room temperature. The splitting of tetragonal peaks is attributed to the Cu $K_{\alpha 1}$ and $K_{\alpha 2}$ radiations in the X-ray source.

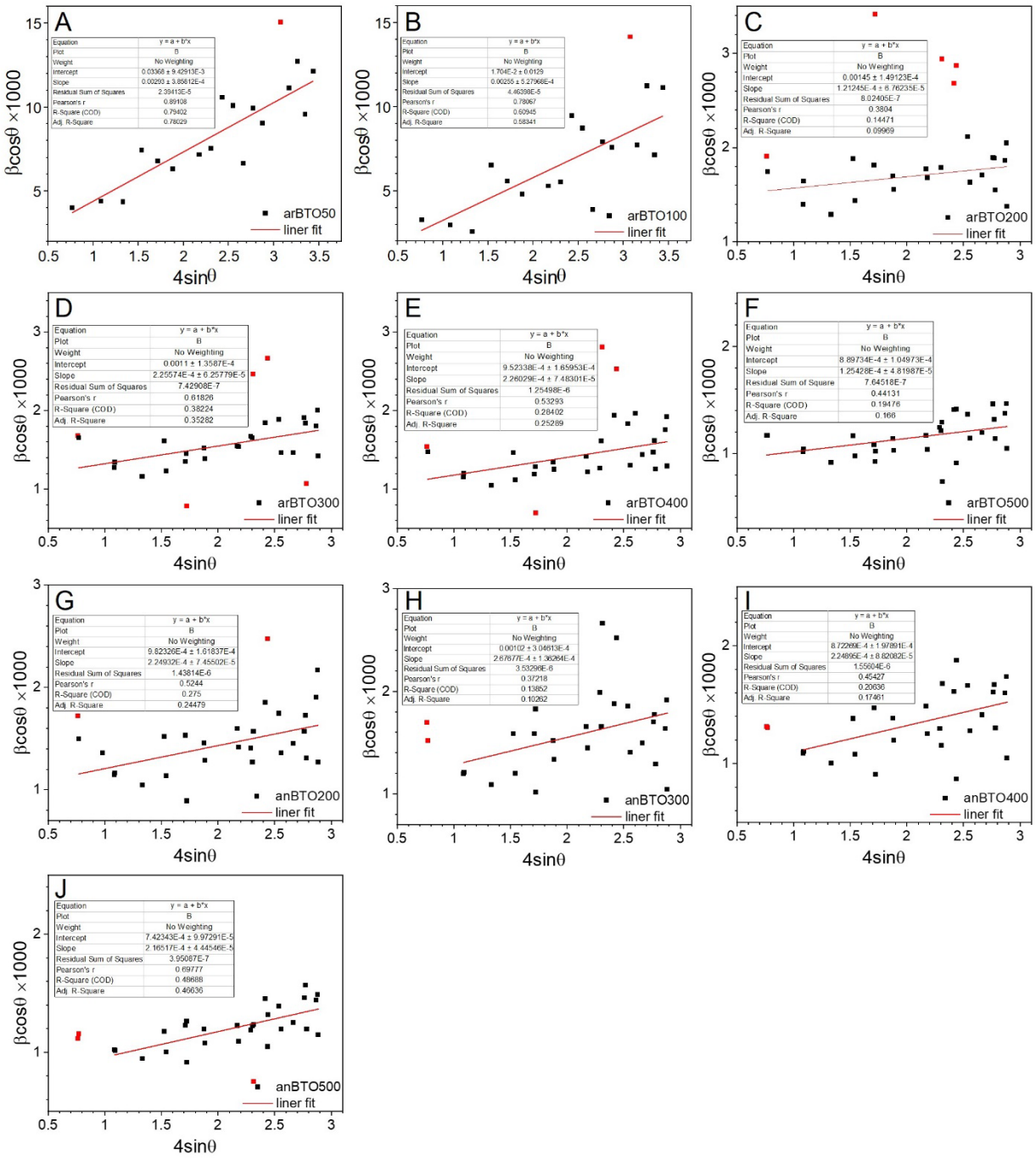

Fig. S11. Williamson-Hall plots for (A) arBTO50, (B) arBTO100, (C) arBTO200, (D) arBTO300, (E) arBTO400, (F) arBTO500, (G) anBTO200, (H) anBTO300, (I) anBTO400, and (J) anBTO500. The red data points are masked for the linear fitting.

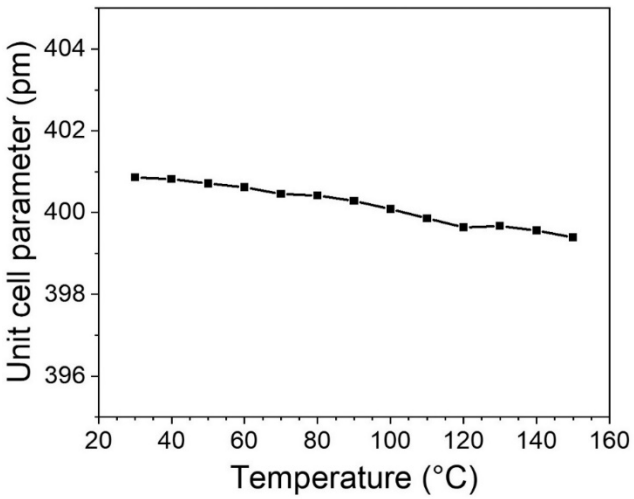

Fig. S12. Unit cell parameter as a function of temperature for arBTO100 during the heating process.

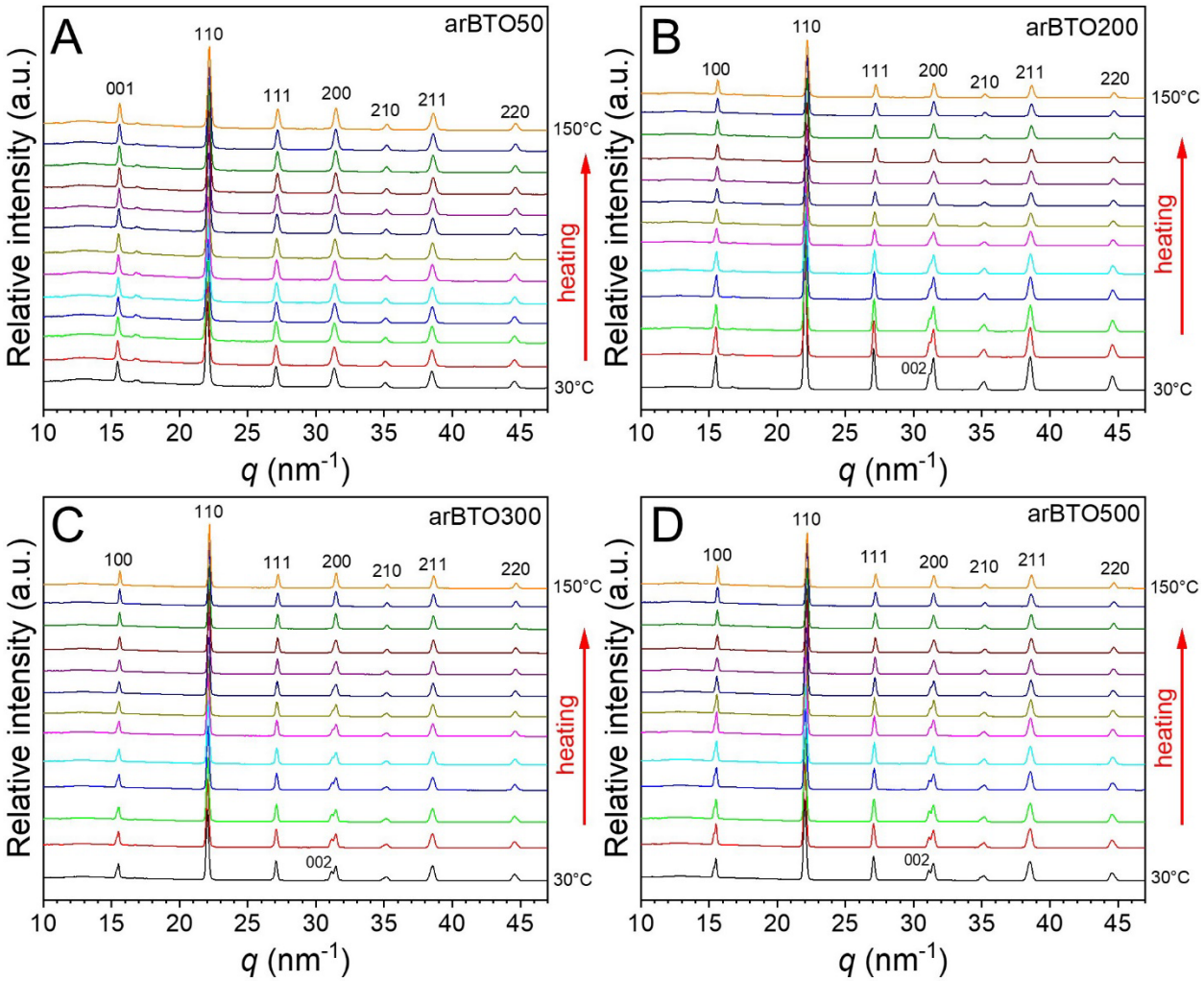

Fig. S13. Temperature-dependent XRD for (A) arBTO50, (B) arBTO200, (C) arBTO300, and (D) arBTO500.

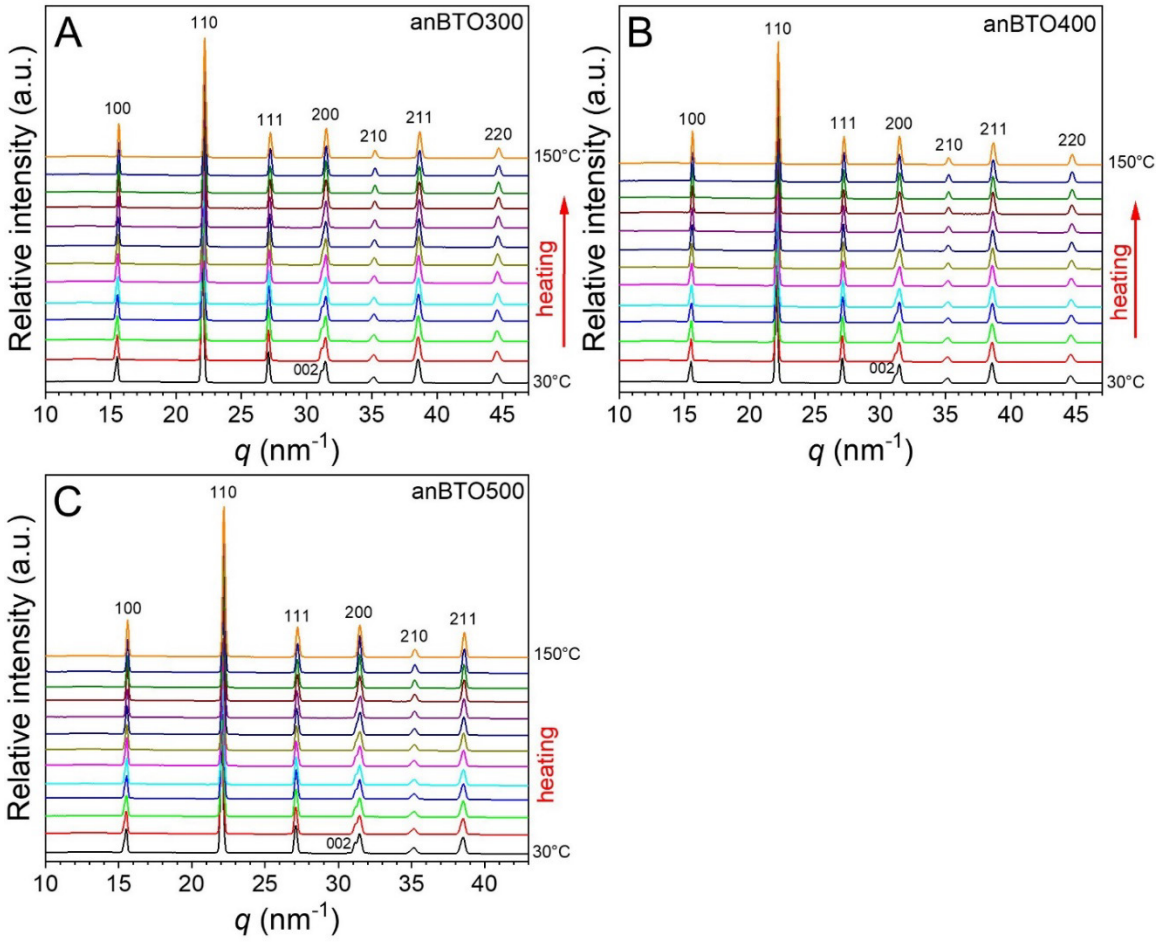

Fig. S14. Temperature-dependent XRD for (A) anBTO300, (B) anBTO400, and (C) anBTO500.

4. Room-temperature Raman of arBTO nanocrystals

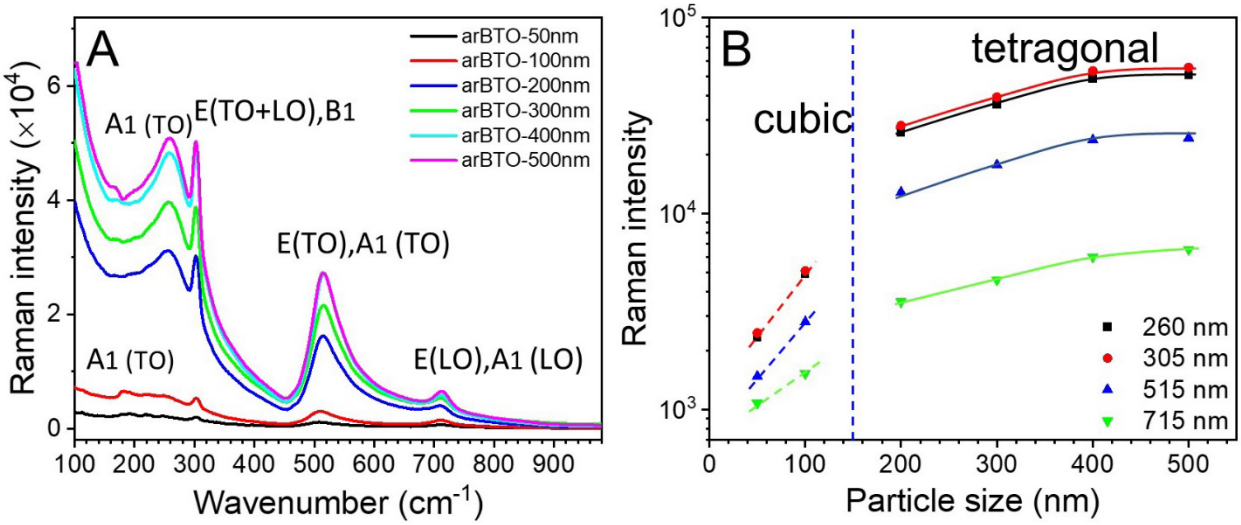

Fig. S15. (A) Raman spectra for arBTO50-arBTO500 nanocrystals in the ambient environment and corresponding peak intensities versus nominal particle size.

5. DSC results of $BaTiO_3$ single crystal and cooling DSC curves of BTO nanocrystals

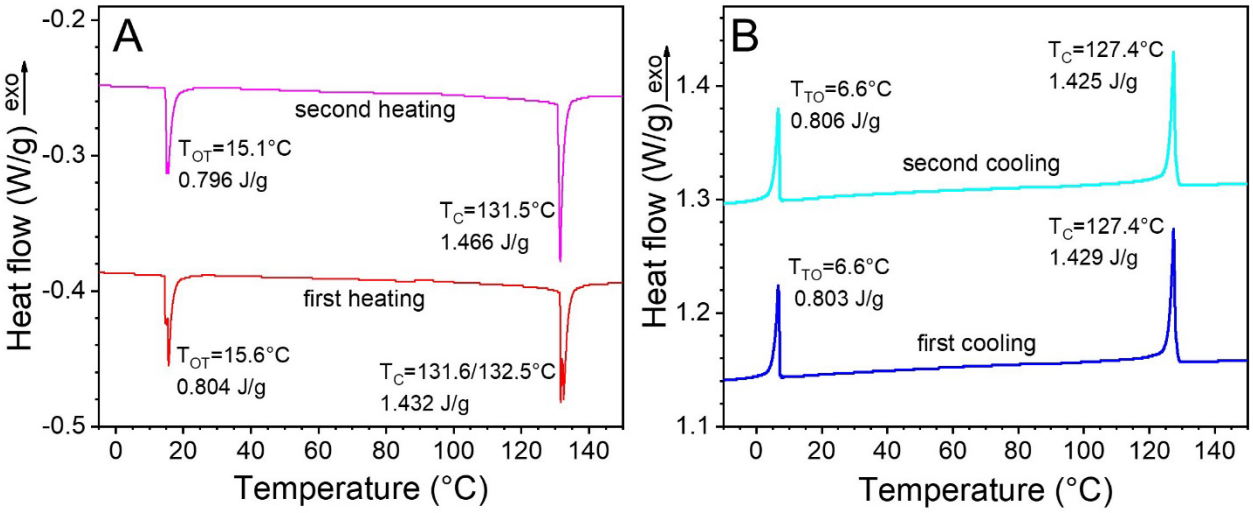

Fig. S16. (A) Heating and (B) cooling DSC curves of the $BaTiO_3$ (001)-single crystal. The heating and cooling rates were 10 °C/min. The sample weight was 10.65 mg.

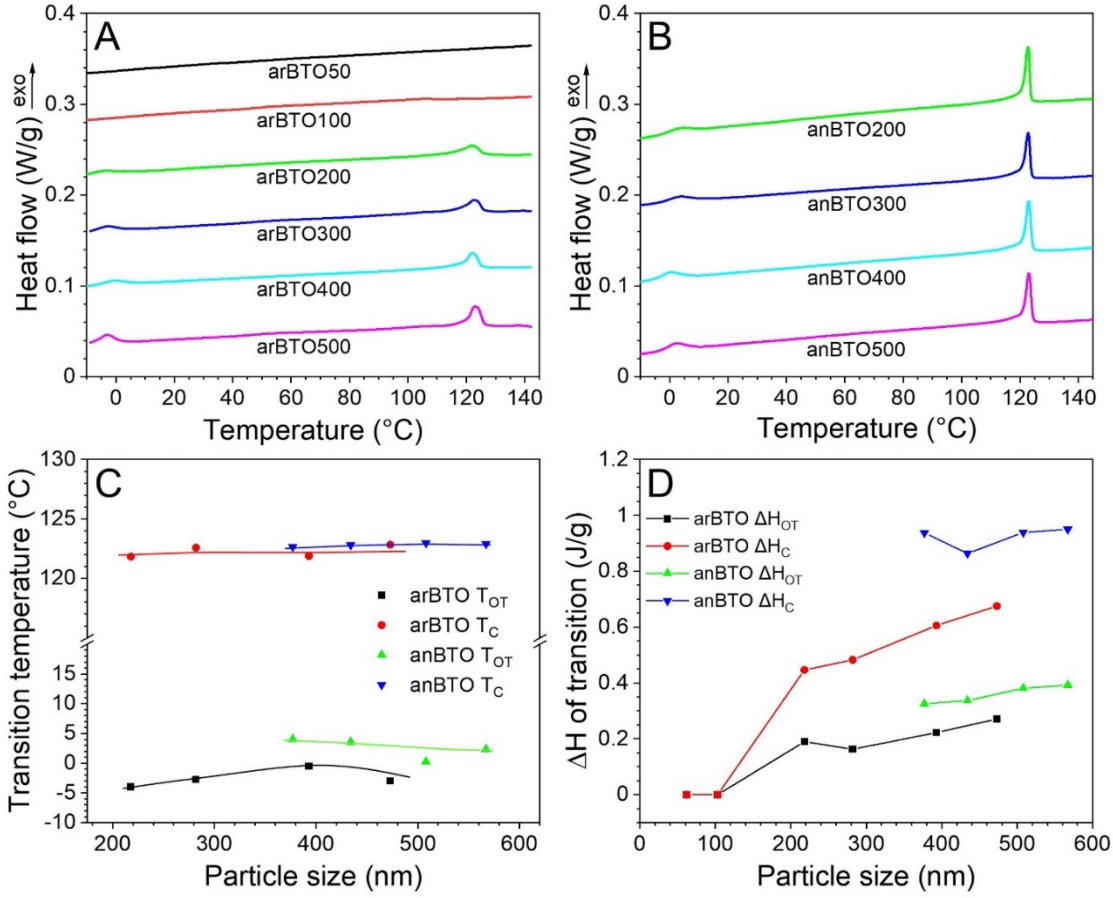

Fig. S17. Cooling DSC curves of (A) arBTO50-arBTO500 and (B) anBTO200-anBTO500 nanocrystals with (C) phase transition temperatures, and (D) heats of transition (ΔH) as a function of the actual particle size.

6. XPS analysis of arBTO and anBTO nanocrystals

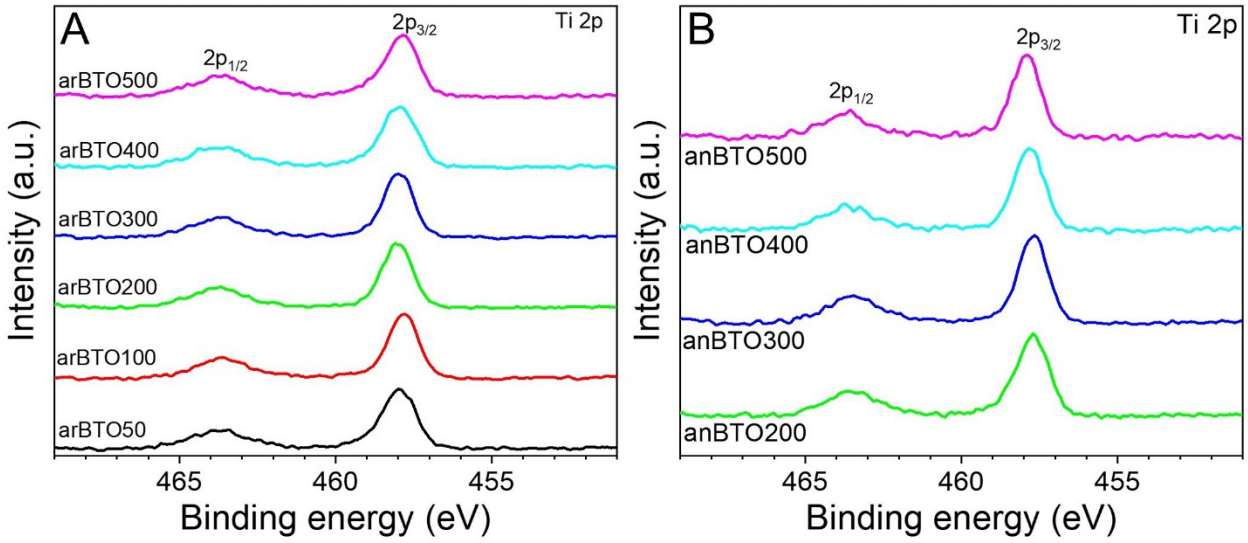

Fig. S18. XPS spectra of Ti 2p peaks for (A) arBTO50-arBTO500 and (B) anBTO200-anBTO500 nanocrystals.

7. High-resolution TEM analysis of arBTO and anBTO nanocrystals

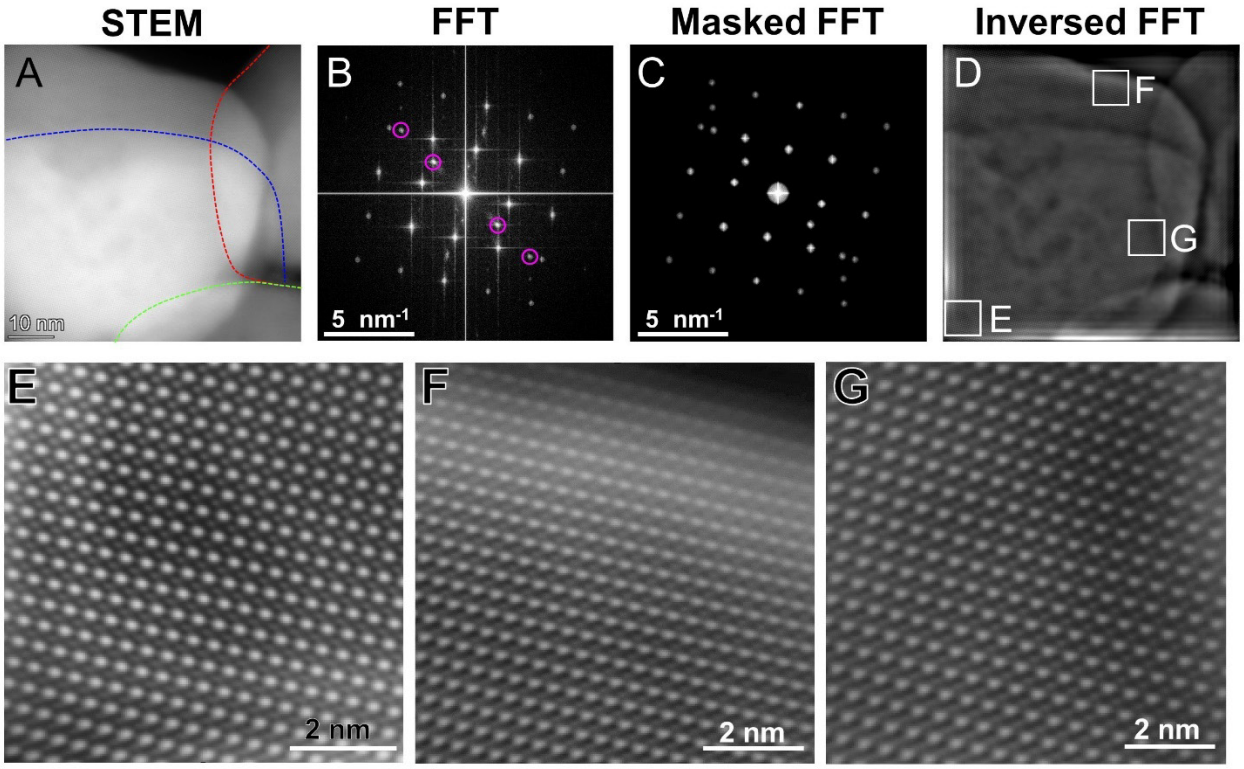

Fig. S19. (A) HAADF STEM micrograph of arBTO50 nanocrystals with (B) FFT pattern, (C) masked FFT pattern, and (D) corresponding inversed FFT image. The (E, F, G) enlarged atomic resolution images are from the white square areas in (D).

The clean diffraction pattern and the iFFT from the same nanoparticle collectively showed that the BTO nanoparticle should be single crystalline. The underlying nanoparticles, which partially overlapped with the primary particle, were marked with dashed lines of different colors in Fig. S19A. By performing the corresponded FFT of the nanoparticle clusters (Fig. S19B), only one extra set of diffraction spots were identified and marked with purple circles, indicating another nanoparticle is close to a diffraction zone. Next, the identified spots were masked (Fig. S19C) and used to generate the iFFT image. Then, brightness and contrast were adjusted to increase the visibility of atom columns (Fig. S19D). Although four nanoparticles could be identified in the iFFT image, only the primary nanoparticle in view and the nanoparticle on its right (originally marked with red dash line) had lattice fringes correlates to (100) planes of cubic $BaTiO_3$. Hence, the particle with red dash lines was close to a diffraction zone to present the circled diffraction spots in Fig. S19B. In addition, with enlarged areas from the different regions of the primary particle (Figs. S19E-G), the unit cells were aligned in the same direction, further proving the single crystalline $BaTiO_3$ nanocrystal.

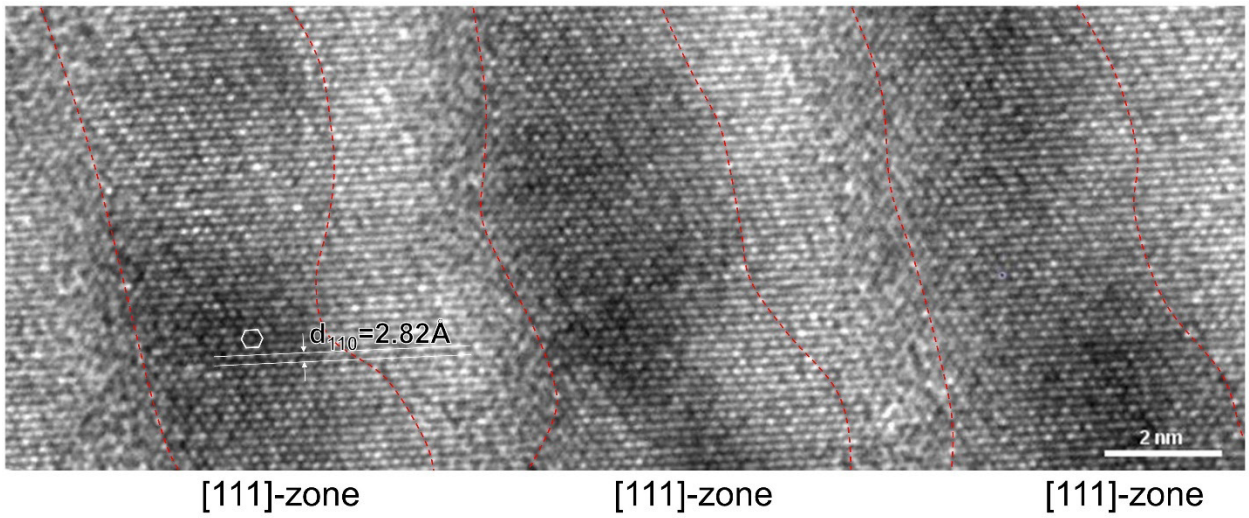

Fig. S20. Enlarged HRTEM of arBTO200 nanocrystal.

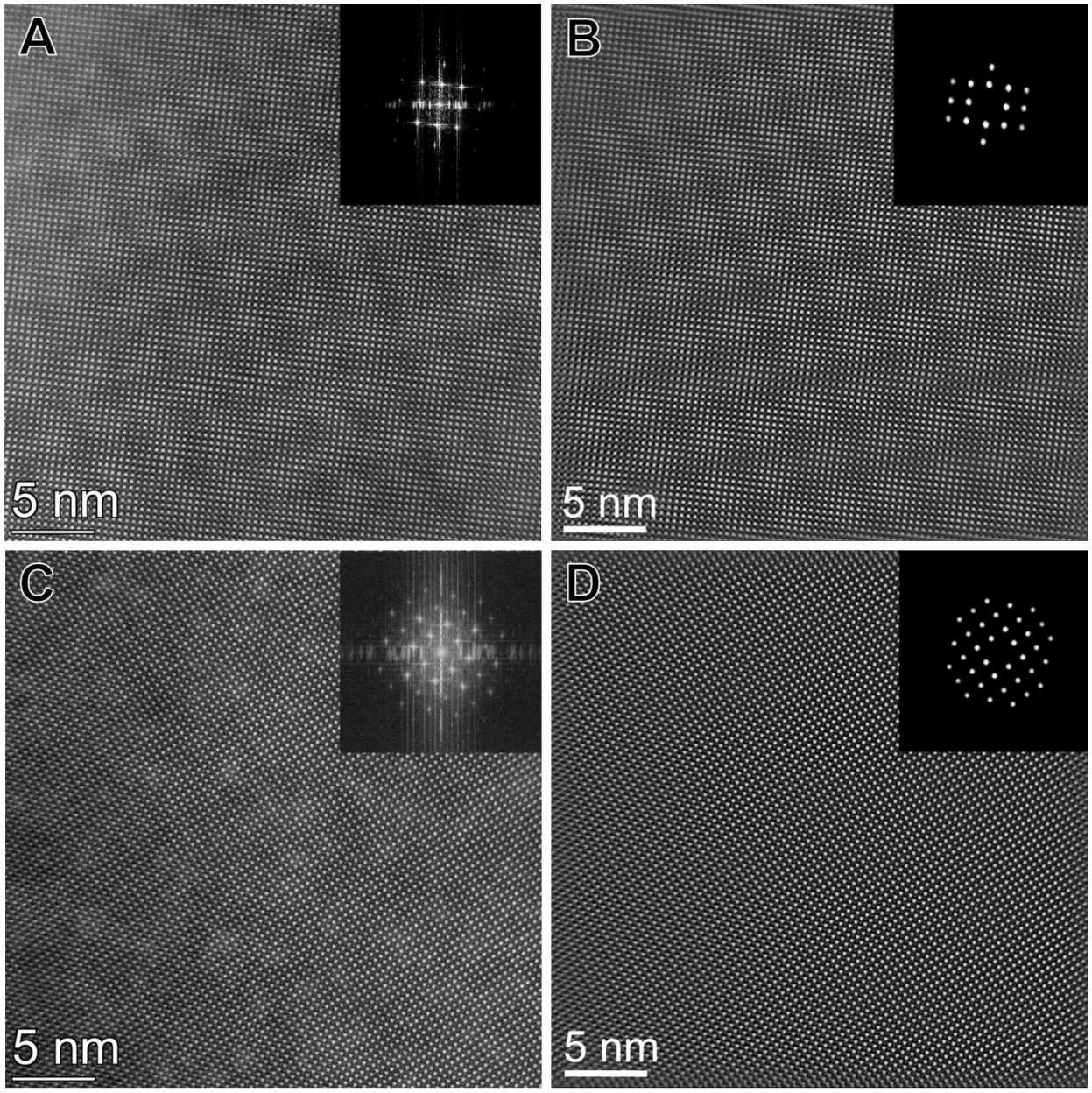

Fig. S21. STEM HAADF micrographs of (A) arBTO200 and (C) anBTO200 nanocrystals with the FFT pattern as insets, and (B, D) iFFT images of (A) and (C) with masked FFT as insets.

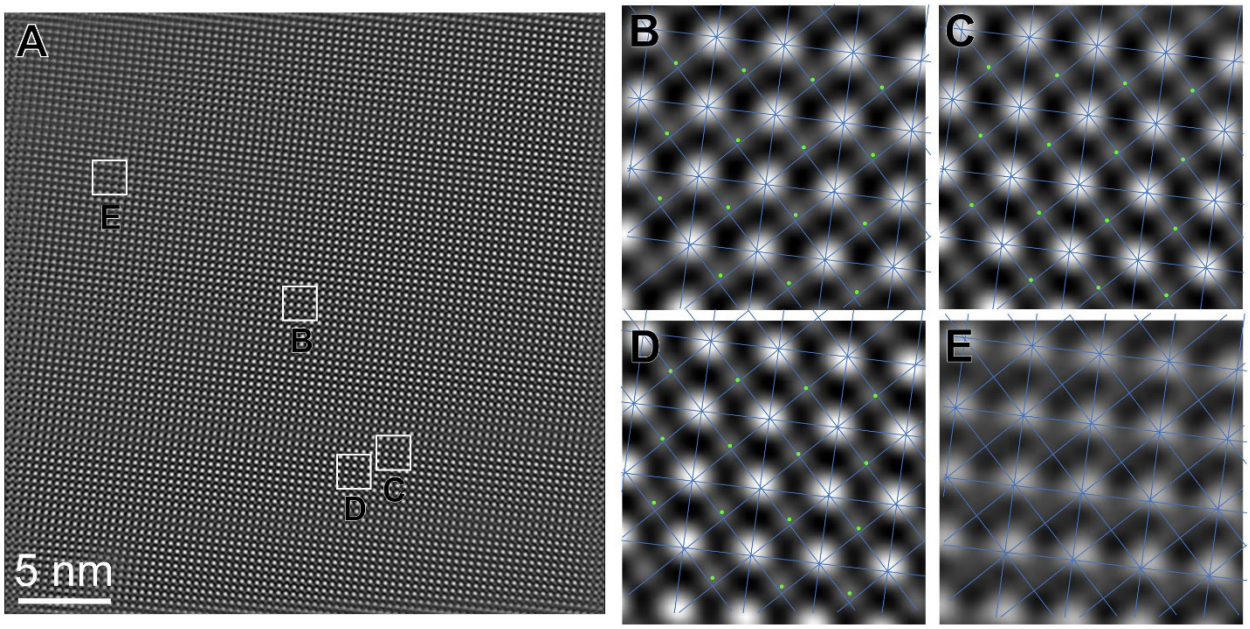

Fig. S22. (A) iFFT image of an arBTO200 nanocrystal and (B-E) enlarged atomic resolution images of selected areas in (A).

8. Linear dielectric properties by BDS

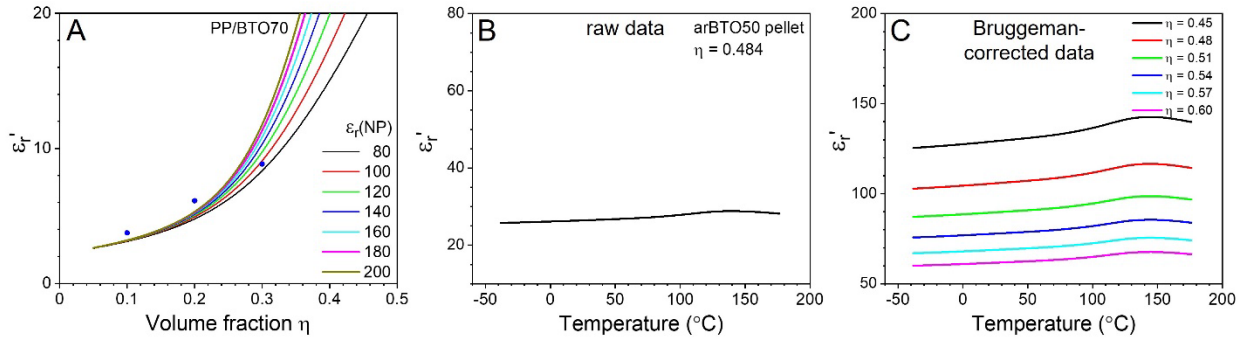

Fig. S23. (A) Dielectric constant (ε_r') versus volume fraction (η) for the PP/BTO70 (70 nm BTO particles) nanocomposites with η = 0.10, 0.20, and 0.30. Bruggeman lines with different BTO dielectric constants from 80 to 200 are shown. (B) Temperature-scan ε_r' for the arBTO50 pellet. (C) Bruggeman-corrected ε_r' curves for the arBTO50 particles with different packing fractions from 0.45 to 0.60.

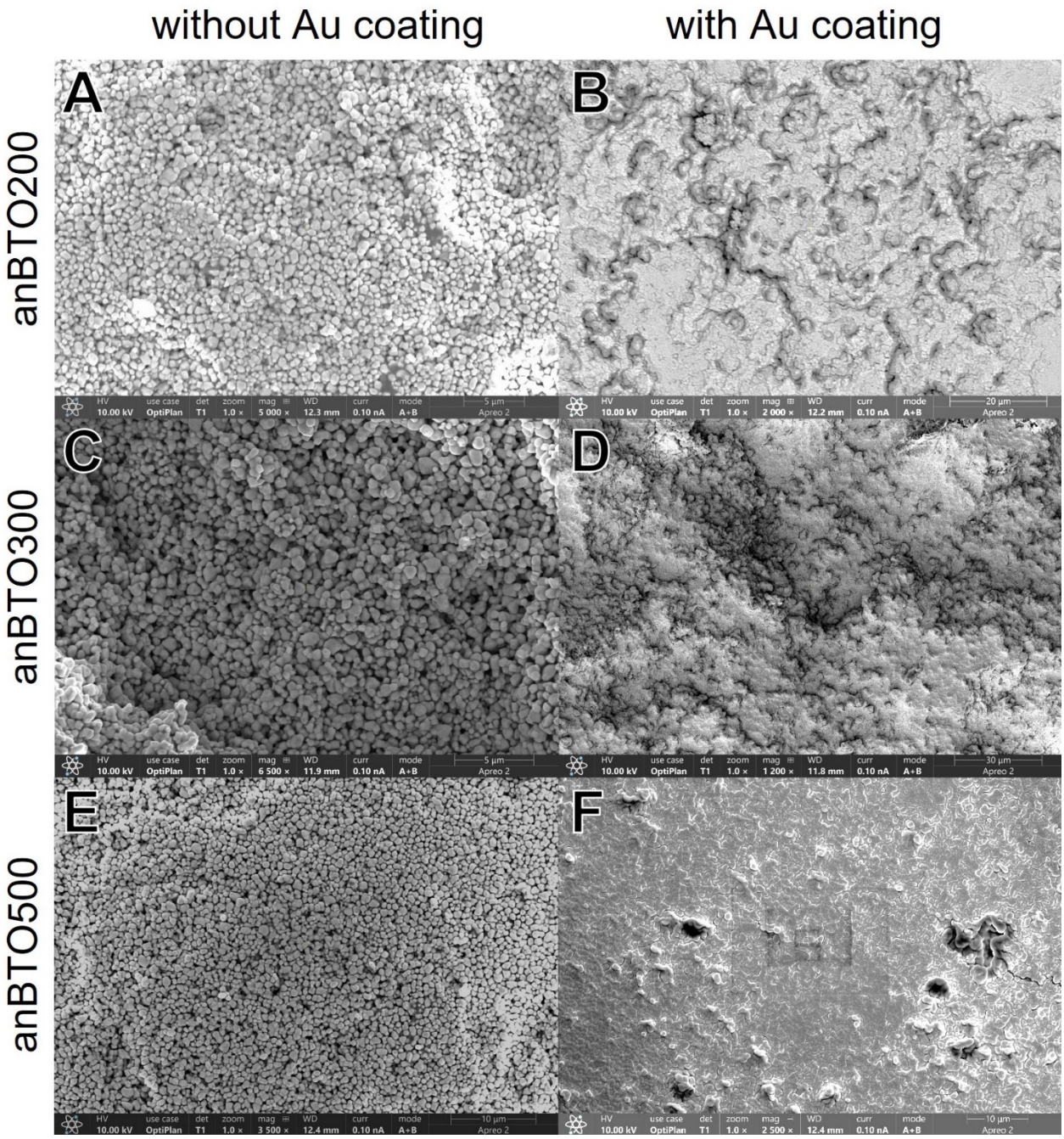

Fig. S24. SEM micrographs for (A,B) anBTO200, (C,D) anBTO300, and (E,F) anBTO500 (A,C,E) without and (B,D,F) with gold (Au) coating.

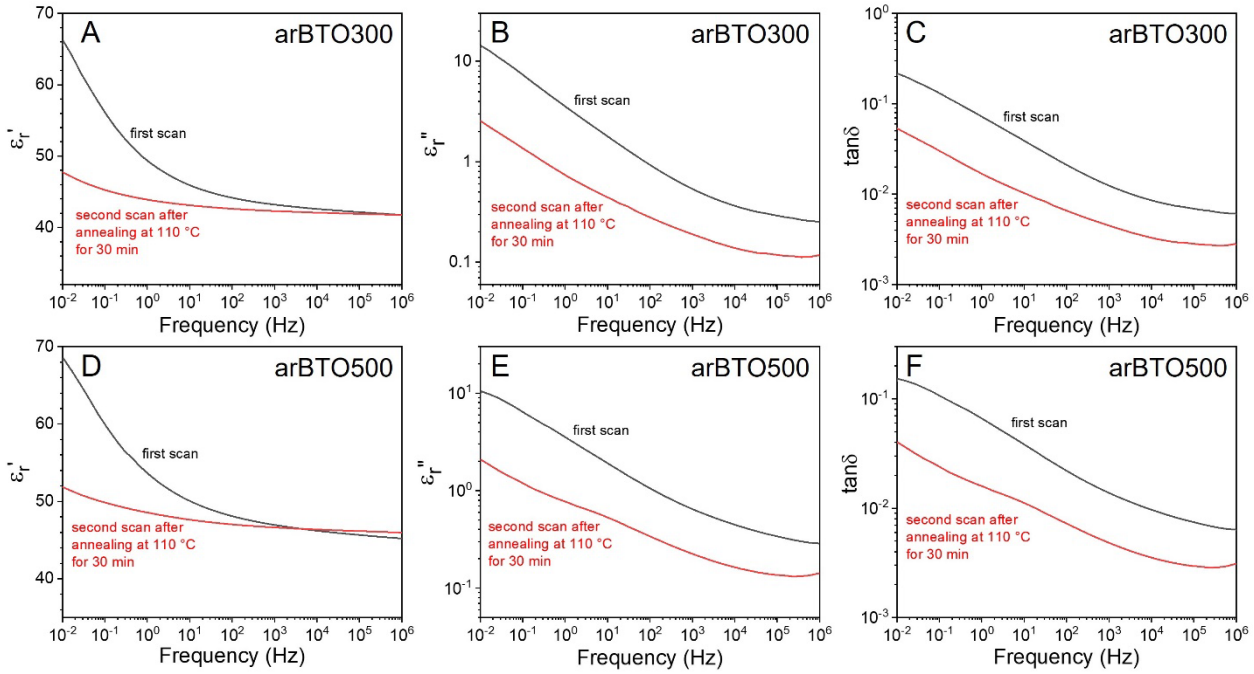

Fig. S25. Frequency-scan BDS results of (A,D) ε_r', (B,E) ε_r'', and (C,F) tanδ for (A-C) arBTO300 and (D-F) arBTO500 before and after annealing at 110 °C to remove moisture.

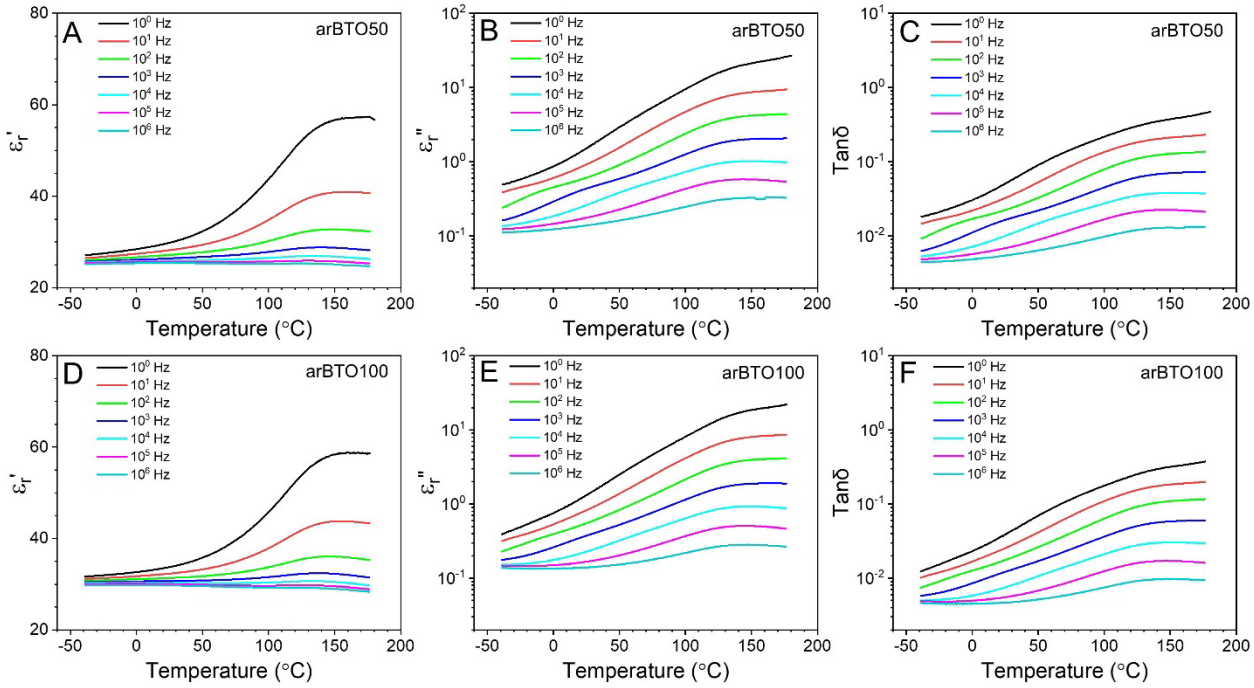

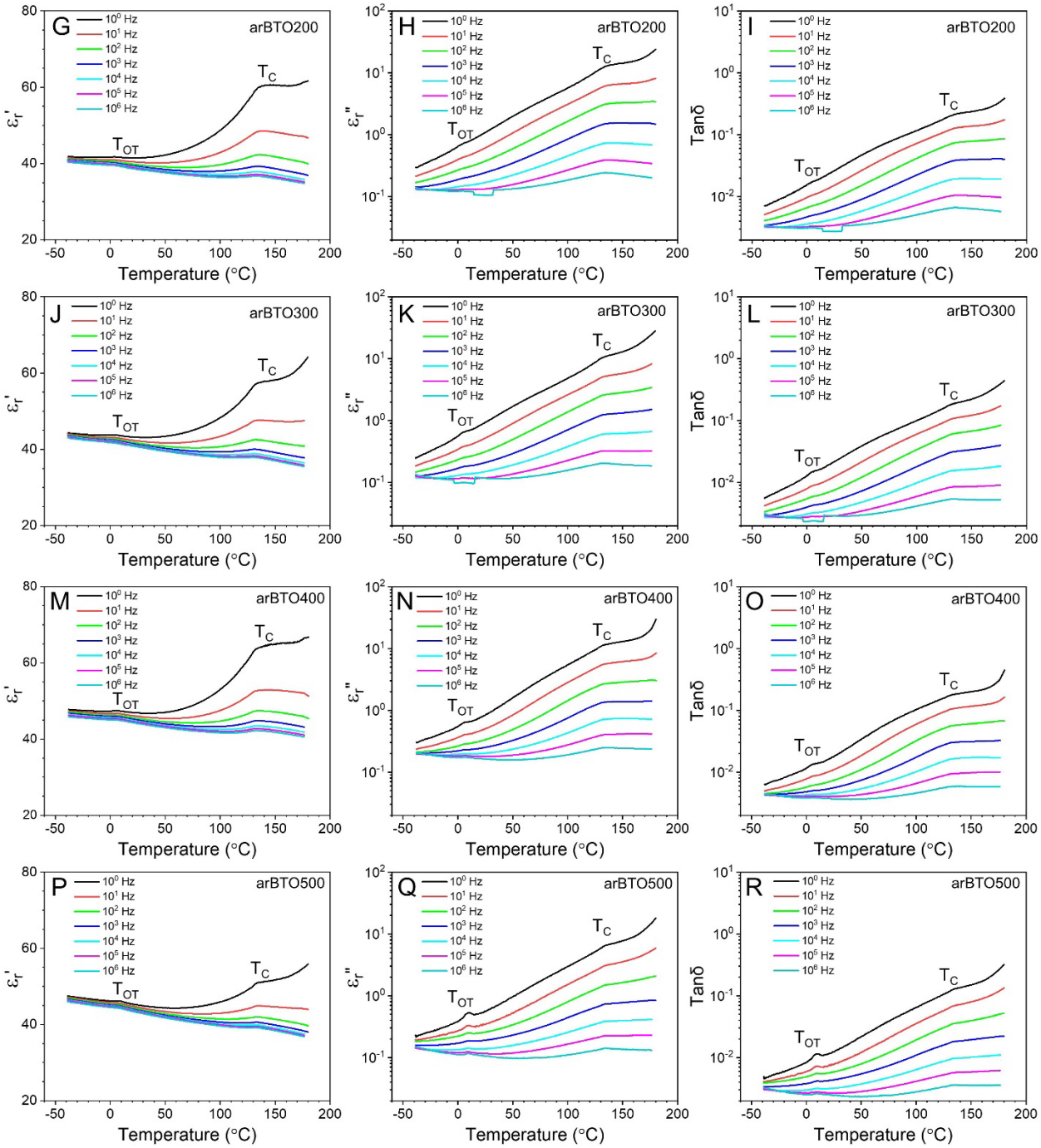

Fig. S26. Temperature-scan BDS results of (A,D,G,J,M,P) ε_r', (B,E,H,K,N,Q) ε_r'', and (C,F,I,L,O,R) tanδ for the hydraulic-pressed arBTO-silicone rubber composites containing (A-C) arBTO50, (D-F), arBTO100, (G-H) arBTO200, (I-K) arBTO300, (L-N) arBTO400, and (O-R) arBTO500 under different frequencies.

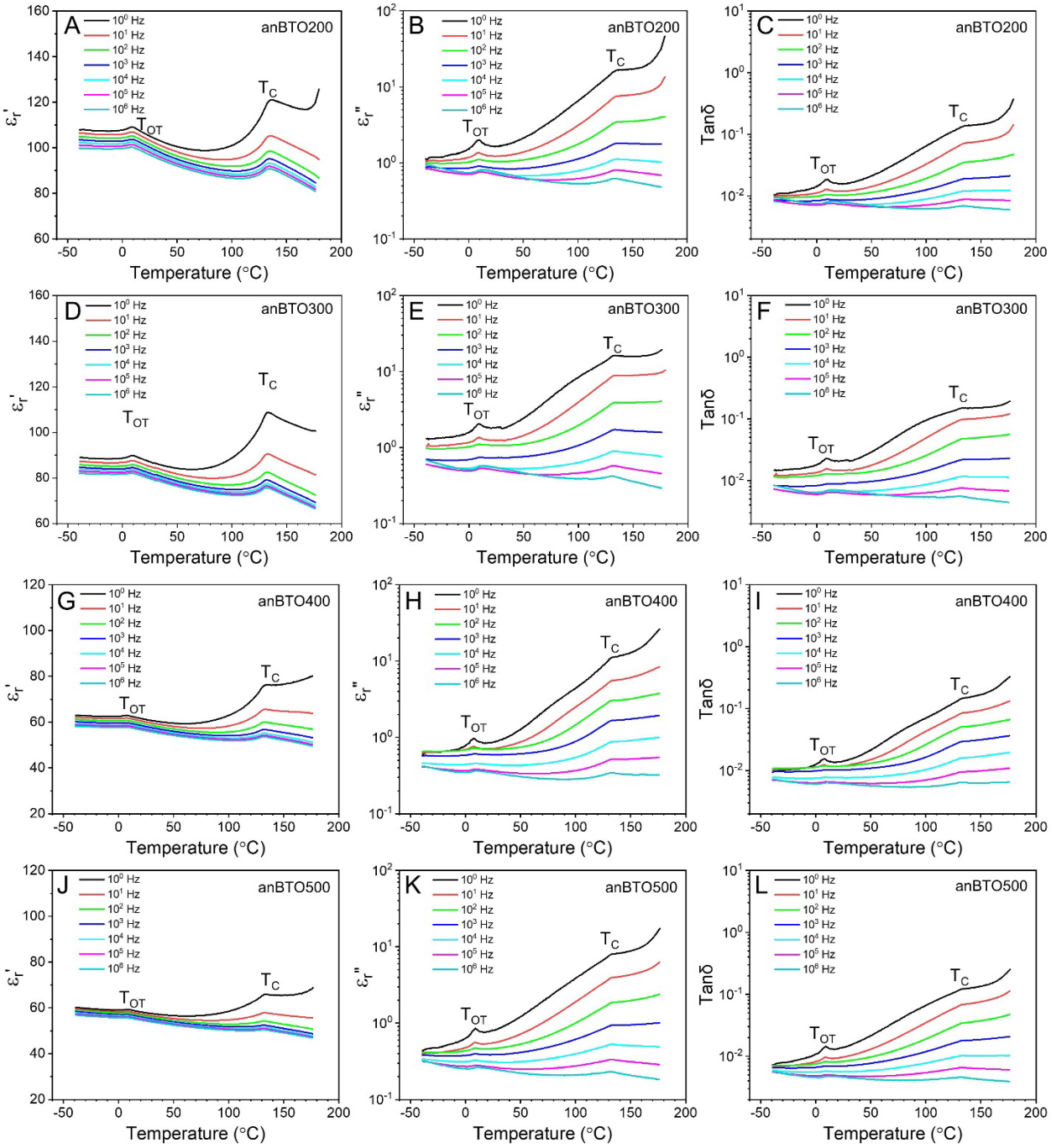

Fig. S27. Temperature-scan BDS results of (A,D,G,J) ε_r', (B,E,H,K) ε_r'', and (C,F,I,L) tanδ for the hydraulic-pressed anBTO-silicone rubber composites containing (A-C) anBTO200, (D-F), anBTO300, (G-H) anBTO400, and (I-K) anBTO500 under different frequencies.

In these figures, the increased ε_r', ε_r'', and tanδ at high temperatures and low frequencies are attributed to the conduction loss from impurity ions, especially at the particle surfaces.

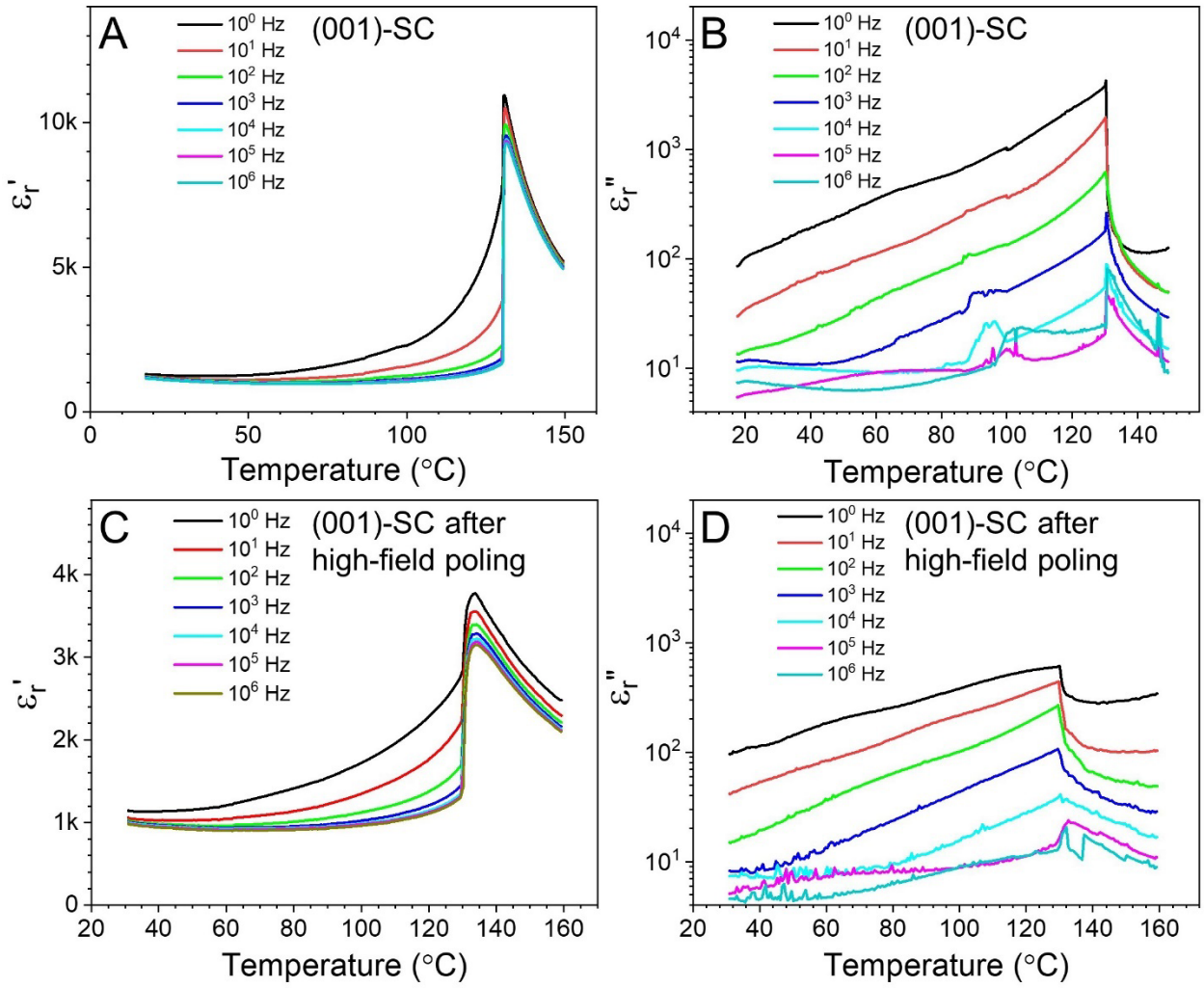

Fig. S28. Temperature-scan BDS results of (A,C) ε_r' and (B,D) ε_r' for the $BaTiO_3$ (001)-single crystal (SC) before and after high-field electric poling (up to 3 MV/m at 10 Hz).

The original $BaTiO_3$ (001)-single crystal exhibited high dielectric constant due to the multidomain nature (Fig. 28A). After repeated electric poling up to 3 MV/m at 10 Hz, the number of domains became smaller. As a result, the dielectric constant decreased, as shown in Fig. 28C.